HAL
open science

Second order Implicit-Explicit Total Variation Diminishing schemes for the Euler system in the low Mach regime

Giacomo Dimarco, Raphaël Loubère, Victor Michel-Dansac, Marie-Hélène Vignal

To cite this version:

Giacomo Dimarco, Raphaël Loubère, Victor Michel-Dansac, Marie-Hélène Vignal. Second order Implicit-Explicit Total Variation Diminishing schemes for the Euler system in the low Mach regime. Journal of Computational Physics, 2018, 372, pp.178 - 201. 10.1016/j.jcp.2018.06.022 . hal-01620627v2

HAL Id: hal-01620627

https://hal.science/hal-01620627v2

Submitted on 5 Nov 2018

HAL is a multi-disciplinary open access archive for the deposit and dissemination of scientific research documents, whether they are published or not. The documents may come from teaching and research institutions in France or abroad, or from public or private research centers.

L'archive ouverte pluridisciplinaire **HAL**, est destinée au dépôt et à la diffusion de documents scientifiques de niveau recherche, publiés ou non, émanant des établissements d'enseignement et de recherche français ou étrangers, des laboratoires publics ou privés.

Second-order Implicit-Explicit Total Variation Diminishing schemes for the Euler system in the low Mach regime

Giacomo Dimarco[a], Raphaël Loubère[b], Victor Michel-Dansac[c], Marie-Hélène Vignal[c]

[a]*Department of Mathematics and Computer Science, University of Ferrara, Ferrara, Italy*
[b]*CNRS and Institut de Mathématiques de Bordeaux (IMB) Université de Bordeaux, France*
[c]*Institut de Mathématiques de Toulouse (IMT), Université P. Sabatier, Toulouse*

Abstract

In this work, we consider the development of implicit-explicit total variation diminishing (TVD) methods (also termed SSP: strong stability preserving) for the compressible isentropic Euler system in the low Mach number regime. The proposed scheme is asymptotically stable with a CFL condition independent of the Mach number. In addition, it degenerates, in the low Mach number regime, to a consistent discretization of the incompressible system. Since it has been proved that implicit schemes of order higher than one cannot be TVD (SSP) [30], we construct a new paradigm of implicit time integrators by coupling first-order in time schemes with second-order ones in the same spirit as highly accurate shock-capturing TVD methods in space. For this particular class of schemes, the TVD property is first proved on a linear model advection equation and then extended to the isentropic Euler case. The result is a method which interpolates from the first- to the second-order both in space and time. It preserves the monotonicity of the solution, and is highly accurate for all choices of the Mach number. Moreover, the time step is only restricted by the non-stiff part of the system. We finally show, thanks to one- and two-dimensional test cases, that the method indeed possesses the claimed properties.

Keywords: Asymptotic Preserving, High-order, IMEX schemes, SSP-TVD, Low Mach, Hyperbolic.

1. Introduction

The analysis [44, 45, 66, 2, 48, 1] and the development of numerical methods [38, 34, 60, 72, 46, 13, 32, 56, 52, 35, 31, 55, 53, 17, 20, 18, 16, 33, 10, 29, 43, 21, 11, 22] for the passage from compressible to incompressible gas dynamics has been and still is a very active field of research. The compressible Euler equations, which describe conservation of density, momentum and energy in a fluid flow, become stiff when the Mach number tends to zero.

In this case, the velocity of the pressure waves is much greater than that of the gas. Thus, a standard model approximation consists in replacing the density conservation equation by a constraint on the velocity divergence, set consequently equal to zero. In addition, using this constraint into the momentum equation gives an elliptic equation for the pressure. We refer to that situation as the incompressible Euler model, which is used to describe many different flow conditions. However, there are situations in which the Mach number may be small in some parts of the domain and large in others, or may strongly change in time. In these cases, one should deal with the coupling of incompressible and compressible regions whose shapes change in time. From the numerical point of view, this causes many difficulties since standard domain decomposition techniques, which couple the solution of the compressible equations with the solution of the incompressible system, may be difficult to use (see [5]). Thus, one solution consists in solving the more complete compressible Euler system in the stiff regime. As a consequence, this introduces strong drawbacks when the Mach number becomes small. The first one is related to the fact that classical explicit schemes for the compressible Euler system are not uniformly stable. Their CFL condition is inversely proportional to the Mach number. This causes

*Corresponding author
Email addresses: giacomo.dimarco@unife.it (Giacomo Dimarco), raphael.loubere@math.u-bordeaux.fr (Raphaël Loubère), Victor.Michel-Dansac@math.univ-toulouse.fr (Victor Michel-Dansac), mhvignal@math.univ-toulouse.fr (Marie-Hélène Vignal)

severe time step limitations in low Mach number regimes. The second drawback is a consistency problem. Indeed, it is well known (see for instance [31, 56, 20, 21]) that explicit Roe type solvers are not consistent in the low Mach number limit. In particular, they fail to describe the limit pressure.

From the physical point of view, it is important to understand that two different situations are possible. In the first situation, sound waves play an important role in the physical problem. Then, even if their velocity is much greater than the one of the fluid, it is crucial to accurately capture these sound waves in this situation. Consequently, the time step of the discretization must be of the order of the Mach number. However, even in these situations, the consistency problems of low Mach regimes should be solved. This problem can be treated by preconditioning and/or pressure correction methods (see above [40, 13, 32, 34, 35, 38, 43, 55, 53, 62, 72, 73]) or AUSM schemes (see [49, 57]).

In this work, we are more interested in the second situation, in which sound waves play a weak role in the physical solution. Consequently, their precise description can be avoided. From the numerical point of view, this means that one would like to use large time steps compared to the small values of the Mach number. However, in order to do that, the scheme should be uniformly stable as well as consistent to the low Mach regimes.
One possible answer to this problem consists in adopting a fully implicit algorithm for the original compressible system. Such approach has been developed in [39] within the framework of multigrid methods. It allows large CFL numbers but it needs a preconditioning procedure to avoid the large number iterations needed for the resolution of the non linear system which originates from the implicit time discretization of the compressible equations [41, 61, 64] Recently, it has been shown that a fully implicit discretization is not the only strategy which permits to get all Mach number schemes. One alternative is represented by asymptotic preserving (AP) schemes [19, 17, 18, 16, 33, 71, 10, 54, 11, 22]. They deal with different models which share the common characteristic of describing a multi-scale dynamic: i.e. a dynamic in which fast and slow scales coexist. These techniques allow computing the solution of such stiff problems while avoiding time step limitations directly related to the fast scale dynamic. This fast scale, in the context of this work, appears in the low Mach number regime when the pressure waves become fast compared to the rest of the dynamic. In addition, these AP methods lead to consistent approximations of the limit model (here the incompressible model) when the parameter which describes the fast scale dynamics goes to zero (here the Mach number). We stress that, even if the proposed methods in this work are specifically designed to avoid the fast scale resolution (remaining uniformly stable), if they are used with small time steps like those necessary for an explicit method, they are able to describe this fast dynamic with high accuracy. Thus, this approach also competitive compared to other methods designed to describe the fast pressure waves.

For the sake of completeness, let us briefly recall the general principle of such schemes. We start from one model of partial differential equations, $\mathcal{M}_\varepsilon$, depending on an arbitrarily small parameter ε and we assume that there exists a limit model, $\mathcal{M}_0$, which describes the dynamic when ε tends to 0. Their respective exact solutions are called $W_\varepsilon(x,t)$ and $W_0(x,t)$ for all space and time position (x,t), see Figure 1 on the left.

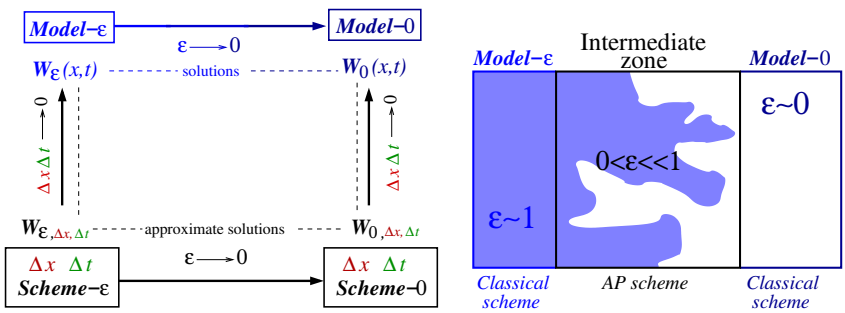

Figure 1: Left: Asymptotic Preserving diagram. The schemes $W_{\varepsilon,\Delta x,\Delta t}$ and $W_{0,\Delta x,\Delta t}$ are consistent discretizations of the models $W_\varepsilon(x,t)$ and $W_0(x,t)$. An Asymptotic Preserving method is such that when $\varepsilon \to 0$, the scheme $W_{\varepsilon,\Delta x,\Delta t}$ automatically becomes the scheme $W_{0,\Delta x,\Delta t}$. Right: An example in which different regimes coexist. While a standard scheme for the $\mathcal{M}_\varepsilon$ model or the $\mathcal{M}_0$ model may only work for large values of ε or when $\varepsilon = 0$, the Asymptotic Preserving scheme works in all regimes and in intermediate regions it is the only one that should be employed.

Classical pairs of such related models are the inviscid Euler equations or the viscous Navier-Stokes model and their low Mach number limits. However, many other examples can be found in the literature, such as the Boltzmann equation and its hydrodynamic limit [23, 24], the shallow-water model and its limit for low Froude numbers, the

Vlasov-Maxwell model in the quasi-neutral limit, hyperbolic systems with stiff source terms, kinetic-fluid models in plasma physics or biology and many others. Here, the square of the Mach number plays the role of the small parameter ε, and when ε tends to zero, compressible flow equations converge to incompressible ones.

From a numerical point of view, on the one hand, if ε is large, standard (or classical) numerical methods can be employed. Such methods are often explicit in time. On the other hand, if $\varepsilon = 0$, then standard (or classical) methods for the limit model can also be employed, see Figure 1 on the right. However, when one has to deal with situations in which the parameter ε which defines the multi-scale nature of the problem varies in time and space, standard numerical methods fail. In these situations, an Asymptotic Preserving method is able to solve the physical problem. With reference to the Figure 1 on the left, it transforms automatically a scheme $W_{\varepsilon,\Delta x,\Delta t}$ for the perturbed model into a scheme $W_{0,\Delta x,\Delta t}$ for the limit model while maintaining the same order of accuracy. However, even if these schemes are designed to deal with multi-scale dynamics, we stress that, in general, their use it is not limited to the intermediate regimes but instead they work in all regimes producing highly accurate results also in the two limits.

It is important to note that the nature of the model $\mathcal{M}_\varepsilon$ for $\varepsilon > 0$ may be different form the one of the model $\mathcal{M}_0$. For instance, one can be hyperbolic and the other parabolic or elliptic. As a consequence, their respective numerical approximations can be substantially different, causing the derivation of such a method hard to be realized. In fact, one scheme can be well suited to solve an hyperbolic model but not necessarily a parabolic or elliptic one. This problem is called the problem of asymptotic consistency. In a same way, even if small amplitude waves (in our case sound waves) are negligible and have a minor impact on the numerical solution, they may lead to very stiff constraints on the time and space steps. This problem is known as asymptotic stability. The stability region of a standard scheme can be reduced to an empty set when ε tends to 0.

Moreover, in realistic configurations, the parameter ε may depend on space and time. It could be large in some parts of the computational domain, and, simultaneously, extremely small in other parts. These regions in which different regimes interact may also vary with time. If one does not want to manage a complicated interface between models, the resolution of the model $\mathcal{M}_\varepsilon$ seems to be the only possible strategy since $\mathcal{M}_\varepsilon$ is the only model valid for all values of ε.

Finally, we want to stress that all these remarks remain true for models closer to the physical reality such as complete Euler model or Navier-Stokes model. In addition, while the complete Euler model introduces additional difficulties in the development of such numerical methods, this appears not to be the case with Navier-Stokes. In fact, we believe that the diffusive term of the Navier-Stokes model will probably simplify the derivation of a scheme based on the same characteristics. In these situations, it is known that that the diffusive term helps in regularizing the solution and thus we expect that the problem of numerical oscillations to be much less pronounced than in the case of Euler equations or to be completely absent.

Note that, as already mentioned, if one is not interested in the resolution of small amplitude waves, it is possible to drop them using an AP scheme and large time steps. In this case, the scheme will only capture the limit solution of the model $\mathcal{M}_0$ and not the small details of the solution of $\mathcal{M}_\varepsilon$ for $\varepsilon \simeq 0$. As an illustration, we report in Figure 2 the one dimensional numerical solutions of the isentropic Euler equation provided by a first-order classical explicit scheme (CL in red) versus our first-order Asymptotic Preserving scheme (AP in blue) for different values of the Mach number, see [22] for the description of these first-order schemes. The test case consists in four Riemann problems with a time varying Mach number $M = \sqrt{\varepsilon}$ showed on the embedded panels. It is important to note that the explicit scheme works only for time steps smaller than the inverse of the Mach number (otherwise, its solution explodes), while the AP method works for larger time steps. Although the classical explicit scheme can capture the small scale features, it demands large computational resources when the Mach number becomes small; 1135 time steps are needed to reach the final time, while the AP scheme requires only 135 time steps. Moreover, when the time steps are comparable, the AP scheme describes the numerical solution as well as the explicit method (see the right panel of Figure 2). Finally, for small ε, when the time step is much larger than the inverse of the Mach number, the AP method projects the solution over the solution of the limit model (see the middle panel). It neglects the small features and saves a large amount of resources.

The work in this paper participates to the effort to develop accurate and robust Asymptotic Preserving numerical schemes. It is based on a first-order asymptotic preserving method developed in a recent work [22], which dealt with an analysis of the stability properties, which led to a stability restriction on the numerical method independent of the Mach number. The L^2- and L^∞ properties of the method have been analyzed in detail.

In the present work, we extend the previous study to the second-order accuracy in time and space. We first

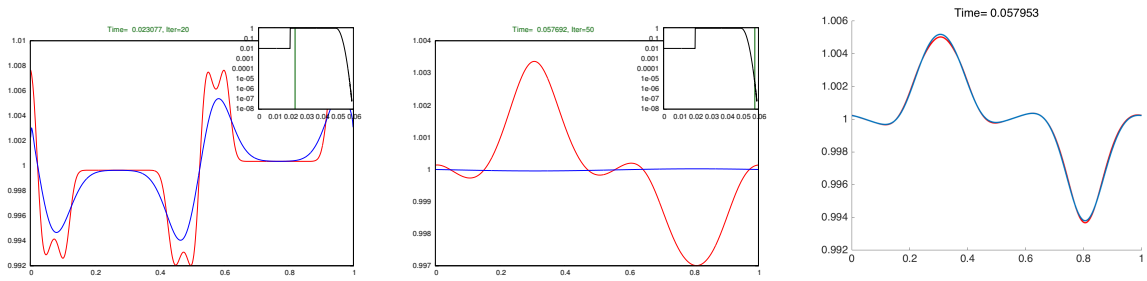

$N_{\text{cycle, CL}} = 43$, $N_{\text{cycle, AP}} = 60$
Ratio 0.7

$N_{\text{cycle, CL}} = 1135$, $N_{\text{cycle, AP}} = 135$
Ratio 8.4

$N_{\text{cycle, AP}} = N_{\text{cycle, CL}}$,
$\varepsilon \approx 1.8 \times 10^{-6}$

Figure 2: Illustration of the behavior of a classical explicit scheme (red) and an Asymptotic Preserving scheme (blue) solving a Riemann like problem with 600 cells for time varying Mach number M, the squared value of which is represented on the embedded top panels as a function of time. Density is shown as a function of space for two intermediate times. — Left panel: when M is large enough, the same global solution is captured with almost the same computational effort. The AP scheme is more diffusive than the classical explicit one. Middle panel: when M becomes small, the AP scheme captures the limit solution and spares some computational resources. Right panel: same time and Mach number as the middle panel, the AP scheme uses the explicit time steps: both schemes give similar results.

present an L^2-stable second-order extension of our previous method. Then, since it has been proved in [30] that the L^∞-stability and Total Variation Diminishing (TVD, also named Strong Stability Preserving, SSP) properties cannot be ensured for an unconstrained implicit in time scheme of order greater than one, we construct a new paradigm of highly accurate implicit in time schemes. Several studies on IMEX-SSP methods or Implicit-SSP methods have been proposed in recent years [28, 37, 42, 15, 36, 68, 9]. In all these articles, authors look for the largest possible time step allowing the SSP property to be preserved. We stress that, in the present work, we do not pursue in this direction since the stiffness of the equations typically requires numerical methods whose time steps are disconnected from the stiff scales, and, possibly, several orders of magnitude larger. As shown in [30], this will not be possible with standard IMEX-SSP methods. For this reason, the direction chosen in this work consists in constructing a TVD Asymptotic Preserving (AP) scheme using a convex combination of first- and second-order implicit-explicit (IMEX) methods in the same spirit as high-resolution shock-capturing TVD methods in space [47, 69]. The resulting TVD-AP scheme possesses both the L^∞- stability and the TVD properties. Moreover, this technique opens the way to the construction of arbitrarily high-order accurate methods with the same properties. Details of this approach and development of high resolution schemes by combining schemes of order higher than two with first-order implicit methods in the case of the linear and nonlinear transport equations are currently under study [51].

In a second part of the work, we discuss limiters. They must detect the problematic situations in which the TVD property no longer holds. In such cases, the scheme must switch from the second-order accurate scheme to the TVD-AP scheme without losing accuracy. The proposed approach is based on the so-called MOOD (Multidimensional Optimal Order Detection) method [12, 25, 26]. It has been originally developed to detect the loss of physical properties when dealing with high-resolution in space methods, and to reduce the order of the space discretization to restore the physical properties of the problem. Here, we extend the previous method to the case of the implicit time discretizations. To summarize, the proposed method ensures a non oscillatory approximation of our original problem, which is more accurate than the one given by a first-order AP scheme, stable independently of the Mach number, and which degenerates to an high-order time-space discretization of the incompressible Euler equations in the limit when the Mach number goes to zero.

The article is organized as follows. In Section 2, we briefly recall the isentropic/isothermal system of Euler equations and its low Mach number limit, as well as the first-order accurate Asymptotic Preserving scheme presented in [22] which is the basis of the second-order extension considered here. Then, in Section 3, we present a second-order in time AP scheme for the isentropic Euler system and we show that, even though it is L^2-stable, it presents some non-physical oscillations when the explicit CFL condition is violated. Thus, in Section 4, we introduce a model problem which will be used to construct a TVD AP scheme for the Euler system, and we study its L^2-stability, L^∞-stability and TVD properties. In Section 5, we extend the previous scheme to the low Mach number case and we introduce the MOOD procedure to detect a loss of L^∞-stability. Finally, in Section 6, we show the good behavior of our AP schemes with different numerical results for three different one-dimensional test cases and two two-dimensional ones.

A concluding section ends the paper.

Let us finally remark that, in this work, we only focus on the isentropic Euler system and its low Mach number limit. However, we stress that most of the difficulties of the all Mach number flows are already present in this simplified model. In fact, the main problem related to the simulation of all Mach flows is due to the presence of two waves which may have completely different speeds. This type of dynamic can be described by the isentropic Euler equations. Thanks to this simplified model, we are able to perform an analysis of the numerical scheme, which can then be extended to the case of the full Euler equations or to the Navier-Stokes model. However, the extension to the full Euler equations is more involved (see [22]), and an in-depth analysis is necessary to construct a scheme which guarantees uniform in time stability and high-order accuracy. For the Navier-Stokes model, we expect a simpler situation. In fact, the implicit treatment of the diffusion term increases the stability of the scheme. This means that we expect the SSP property to be more easily satisfied.

2. The first-order asymptotic preserving scheme for the Euler system in the low Mach number limit

We consider a bounded polygonal domain $\Omega \in \mathbb{R}^d$, where $d \in \{1, 2, 3\}$. The space and time variables are respectively denoted by $x \in \Omega$ and $t \in \mathbb{R}_+$. We study the isentropic/isothermal rescaled Euler model with $\varepsilon > 0$ the squared Mach number (see [44, 50] for instance). It is governed by:

$$\begin{aligned} &\partial_t \rho + \nabla \cdot (\rho U) = 0, \\ &\partial_t (\rho U) + \nabla \cdot (\rho U \otimes U) + \frac{1}{\varepsilon} \nabla p(\rho) = 0, \end{aligned} \tag{1}$$

where $\rho(t, x) > 0$ is the density of the fluid, $U(t, x) \in \mathbb{R}^d$ its velocity, and $p(\rho) = \rho^\gamma$ its pressure. The parameter $\gamma \geq 1$ is the ratio of specific heats, $\gamma = 1$ corresponds to isothermal fluids while $\gamma > 1$ corresponds to isentropic ones.

Equipped with suitable initial and boundary conditions (consistent with the limit model), system (1) tends to the incompressible isentropic/isothermal Euler system when $\varepsilon \to 0$ (see [44, 45, 66, 2, 48, 50, 1] for rigorous results). A formal derivation of this limit is presented for instance in [22]. In the work cited above, the authors introduce well-preparedness and incompressibility assumptions on the initial and boundary conditions and then show that equations (1) tend to the following incompressible Euler equations in the low Mach number limit $\varepsilon \to 0$:

$$\begin{aligned} &\rho = \rho_0, \\ &\nabla \cdot U = 0, \\ &\rho_0 \partial_t U + \rho_0 \nabla \cdot (U \otimes U) + \nabla \pi_1 = 0, \end{aligned} \tag{2}$$

where the first-order correction of the pressure, denoted by π_1, is implicitly defined by the incompressibility constraint $\nabla \cdot U = 0$.

We now briefly recall the numerical method [22] which serves as a basis for the new method introduced in the next section. The discretization of the space and time domains follows the usual finite volume framework. The solution $W(t, x) = (\rho, \rho U)(t, x)$ of the Euler equations is approximated at time $t^n = n\Delta t$, where Δt is the time step, by W^n. The scheme relies on an IMEX (IMplicit-EXplicit) decomposition of system (1) (see [17, 18, 71, 22]): for all $n \geq 0$, the semi-discrete in time form of the scheme reads

$$\frac{W^{n+1} - W^n}{\Delta t} + \nabla \cdot F_e(W^n) + \nabla \cdot F_i(W^{n+1}) = 0. \tag{3}$$

where $F_e(W^n) = (0, \rho^n U^n \otimes U^n)$ and $F_i(W^{n+1}) = (\rho^{n+1} U^{n+1},\ p(\rho^{n+1})/\varepsilon\, \mathbb{I}_2)$, and where F_e is taken explicitly while F_i is taken implicitly. As it is shown in [18, 22], this splitting separates the transport from the sonic part. Both parts are hyperbolic, but the transport part is no longer strictly hyperbolic. All explicit Roe type schemes are constructed with a centered flux and the numerical viscosity gives the upwinding necessary for the stability. In the case of the Rusanov scheme used here ([65, 27]), this numerical viscosity is proportional to the maximum eigenvalue of the Jacobian matrix DF_e relative to the explicit flux F_e, which can vanish. However, it has been shown in [22] that the implicit part of the scheme is sufficient to recover some stability properties. We also recall, see [18, 22], that an interesting

property of such approach is that the resolution of the two equations composing the system can be decoupled. Indeed, in (3), taking the divergence of the momentum equation and inserting it into the mass equation yields:

$$\frac{\rho^{n+1}-\rho^n}{\Delta t} + (\nabla\cdot(\rho U))^n - \Delta t\left(\nabla^2 : (\rho U\otimes U)\right)^n - \frac{\Delta t}{\varepsilon}\left(\Delta p(\rho)\right)^{n+1} = 0, \tag{4a}$$

$$\frac{(\rho U)^{n+1}-(\rho U)^n}{\Delta t} + (\nabla\cdot(\rho U\otimes U))^n + \frac{1}{\varepsilon}\left(\nabla p(\rho)\right)^{n+1} = 0, \tag{4b}$$

where ∇^2 and : are respectively the tensor of second-order derivatives and the contracted product of two tensors. Then, one can solve first the nonlinear equation (4a) which gives the updated density ρ^{n+1}, and then get the updated momentum $(\rho U)^{n+1}$ from (4b). The implicit treatments of the pressure gradient and the mass flux respectively provide the asymptotic consistency and the uniform stability of the scheme [22].

We now present the space discretization, in one space dimension for the sake of clarity. The space domain is assumed to be partitioned in cells of center x_j and size Δx. Then, on $[t^n, t^{n+1})$, the fully discrete version of (4) reads as follows:

$$\frac{W_j^{n+1}-W_j^n}{\Delta t} + \frac{(\mathcal{F}_e)^n_{j+\frac{1}{2}} - (\mathcal{F}_e)^n_{j-\frac{1}{2}}}{\Delta x} + \frac{(\mathcal{F}_i)^{n,n+1}_{j+\frac{1}{2}} - (\mathcal{F}_i)^{n,n+1}_{j-\frac{1}{2}}}{\Delta x} - \Delta t\begin{pmatrix}\left(\Delta(\rho u^2)\right)^n_j + \frac{1}{\varepsilon}\left(\Delta p(\rho)\right)^{n+1}_j \\ 0\end{pmatrix} = 0, \tag{5}$$

with u the velocity of the fluid in the x-direction. The explicit numerical flux is given by

$$(\mathcal{F}_e)^n_{j+\frac{1}{2}} := \frac{F_e(W_j^n) + F_e(W_{j+1}^n)}{2} + (\mathcal{D}_e)^n_{j+\frac{1}{2}}(W_{j+1}^n - W_j^n), \tag{6}$$

with $(\mathcal{D}_e)^n_{j+\frac{1}{2}}$ the explicit viscosity coefficient, taken as half of the maximum explicit eigenvalue and given by $(\mathcal{D}_e)^n_{j+\frac{1}{2}} := \max\left(|u_j^n|, |u_{j+1}^n|\right)$. The implicit numerical flux is given by

$$(\mathcal{F}_i)^{n,n+1}_{j+\frac{1}{2}} := \frac{F_i(W_j^{n,n+1}) + F_i(W_{j+1}^{n,n+1})}{2} + (\mathcal{D}_i)^n_{j+\frac{1}{2}}(W_{j+1}^{n+1} - W_j^{n+1}), \tag{7}$$

where $W_j^{n,n+1} = (\rho_j^{n+1}, (\rho u)_j^n)$ and $(\mathcal{D}_i)^n_{j+\frac{1}{2}}$ is the implicit viscosity coefficient, taken as half of the maximum implicit eigenvalue $(\mathcal{D}_i)^n_{j+\frac{1}{2}} := \frac{1}{2}\max\left(\sqrt{p'(\rho_j^n)/\varepsilon}, \sqrt{p'(\rho_{j+1}^n)/\varepsilon}\right)$. This choice for the implicit viscosity is enough to get an L^∞-stable scheme. However, by relaxing this constraint and by fixing the implicit viscosity to zero, one can show that an L^2-stable scheme is obtained. Finally, the second-order derivatives are approximated by classical second-order centered differences while the time step is constrained by the following uniform CFL condition:

$$\Delta t \le \frac{\Delta x}{\max_j\left(2|u_j^n|\right)}. \tag{8}$$

Note that $2u$ corresponds to the first eigenvalue of the explicit flux and, as expected, this CFL condition does not depend on the squared Mach number ε. When ε tends to 0, this scheme yields a consistent discretization of the incompressible system (2). In the following sections, we discuss an extension of this method to the case of high-order time and space discretizations.

3. A second-order asymptotically accurate scheme for the isentropic Euler equations

The second-order in time extension of the method described in the previous section is based on an Implicit-Explicit (IMEX) Runge-Kutta approach [3, 58, 59, 23, 6, 24, 7, 4]. In particular, we make use of the second-order Ascher, Ruuth and Spiteri [3] time discretization denoted from now on by ARS(2,2,2). Let us observe that this discretization has been originally constructed to obtain an AP scheme for convection-diffusion equations and, in particular, to deal with cases where the diffusion (the fast scale) is taken implicit while the convection is explicit. In our case, the

problem is different, since the fast and the slow scales are both of hyperbolic type. This causes a real challenge from the numerical point of view. In fact, as already mentioned, implicit methods of order higher than one for hyperbolic problems cannot be TVD [30]. The situation does not change when implicit-explicit methods are employed, as shown later. It is certainly possible to adapt the SSP methods (see [9, 14, 30, 36, 42, 68]) or in general higher order implicit-explicit time discretizations to our AP-TVD framework in order to further increase the accuracy of the methods for intermediate values of the Mach number. However, the main purpose of this work is to verify the possibility to obtain a scheme which is uniformly stable in time, that preserves the AP properties and that is essentially TVD. The extension of such approach to the general case of high-order IMEX methods is the subject of a future work. Therefore, we use one of the simplest IMEX second-order time discretization for this proof of principle. t is important to note that for IMEX-SSP methods the time steps allowing the TVD property are of the order of explicit time integrators. Unfortunately, these methods are not uniformly stable in the low Mach regime. Indeed, we recall that we are dealing with a limit problem, we look for a method which preserves the TVD property independently of the Mach number, which could possibly be zero. Thus, in order to bypass this problematic situation, the idea, explored in this work, consists in blending together first- and second-order implicit time-space discretizations. This gives rise to a new class of high-resolution in time methods guaranteeing the preservation of the L^∞-stability and TVD properties. Here, we refer to [51] for the construction of general TVD high resolution implicit-explicit time discretizations.

The Butcher tableau of the considered ARS(2,2,2) discretization is detailed in Table 1, with $\beta = 1 - \sqrt{2}/2$ and $\alpha = 1 - 1/(2\beta)$. Note that the explicit tableau applied to the flux F_e is reported on the left, while the implicit tableau applied to the flux F_i is on the right.

$$
\begin{array}{c|ccc}
0 & 0 & 0 & 0 \\
\beta & \beta & 0 & 0 \\
1 & \alpha & 1-\alpha & 0 \\
\hline
 & \alpha & 1-\alpha & 0
\end{array}
\qquad\qquad
\begin{array}{c|ccc}
0 & 0 & 0 & 0 \\
\beta & 0 & \beta & 0 \\
1 & 0 & 1-\beta & \beta \\
\hline
 & 0 & 1-\beta & \beta
\end{array}
$$

Table 1: Butcher tableaux for the ARS(2,2,2) time discretization. Left panel: explicit tableau. Right panel: implicit tableau. $\beta = 1 - \frac{\sqrt{2}}{2}$, $\alpha = \beta - 1$.

Remarking that $\alpha = \beta - 1$ (and so $1 - \alpha = 2 - \beta$), the corresponding semi-discretization of the Euler system is given by

$$
\frac{W^\star - W^n}{\Delta t} + \beta \nabla \cdot F_e(W^n) + \beta \nabla \cdot F_i(W^\star) = 0, \tag{9a}
$$

$$
\frac{W^{n+1} - W^n}{\Delta t} + (\beta - 1) \nabla \cdot F_e(W^n) + (2 - \beta) \nabla \cdot F_e(W^\star) + (1 - \beta) \nabla \cdot F_i(W^\star) + \beta \nabla \cdot F_i(W^{n+1}) = 0. \tag{9b}
$$

Likewise, for the first-order accurate scheme, the previous second-order accurate discretization has an uncoupled formulation. Let us first establish the first step (9a). Taking the divergence of the momentum equation of (9a) and inserting the value of $\nabla \cdot (\rho U)^\star$ into the mass equation of (9a) yields the following uncoupled formulation:

$$
\frac{W^\star - W^n}{\Delta t} + \beta \nabla \cdot F_e(W^n) + \beta \nabla \cdot F_i(W^{n,\star}) - \beta^2 \Delta t \begin{pmatrix} \nabla^2 : (\rho U \otimes U)^n + \dfrac{1}{\varepsilon} \Delta p(\rho^\star) \\ 0 \end{pmatrix} = 0,
$$

where $W^{n,\star} = (\rho^\star, (\rho U)^n)$. Using now the same notation as in the previous section for the first-order accurate scheme, the fully discrete uncoupled first step in one dimension is given by

$$
\frac{W_j^\star - W_j^n}{\Delta t} + \beta \frac{(\mathcal{F}_e)^n_{j+\frac{1}{2}} - (\mathcal{F}_e)^n_{j-\frac{1}{2}}}{\Delta x} + \beta \frac{(\mathcal{F}_i)^{n,\star}_{j+\frac{1}{2}} - (\mathcal{F}_i)^{n,\star}_{j-\frac{1}{2}}}{\Delta x} - \beta^2 \Delta t \begin{pmatrix} \left(\Delta(\rho u^2)\right)^n_j + \dfrac{1}{\varepsilon} \left(\Delta p(\rho)\right)^\star_j \\ 0 \end{pmatrix} = 0. \tag{10a}
$$

We turn to the uncoupled formulation of the second step (9b). We insert the divergence of (ρU^{n+1}), obtained with the

momentum equation of (9b), into the mass equation of (9b). This yields

$$\frac{W^{n+1}-W^n}{\Delta t} + (\beta-1)\,\nabla\cdot F_e(W^n) + (2-\beta)\,\nabla\cdot F_e(W^\star) + (1-\beta)\,\nabla\cdot F_i(W^\star) + \beta\,\nabla\cdot F_i(W^{n,n+1})$$
$$-\beta\,\Delta t\begin{pmatrix}(\beta-1)\,\nabla^2:(\rho U\otimes U)^n + (2-\beta)\,\nabla^2:(\rho U\otimes U)^\star + \dfrac{(1-\beta)}{\varepsilon}\,\Delta p(\rho^\star) + \dfrac{\beta}{\varepsilon}\,\Delta p(\rho^{n+1})\\ 0\end{pmatrix} = 0.$$

Using the same notation as before, the fully discretized second step in one dimension is given by

$$\begin{aligned}\frac{W_j^{n+1}-W_j^n}{\Delta t} &+ (\beta-1)\,\frac{(\mathcal{F}_e)^n_{j+\frac12}-(\mathcal{F}_e)^n_{j-\frac12}}{\Delta x} + (2-\beta)\,\frac{(\mathcal{F}_e)^\star_{j+\frac12}-(\mathcal{F}_e)^\star_{j-\frac12}}{\Delta x}\\ &+(1-\beta)\,\frac{(\mathcal{F}_i)^{\star,\star}_{j+\frac12}-(\mathcal{F}_i)^{\star,\star}_{j-\frac12}}{\Delta x} + \beta\,\frac{(\mathcal{F}_i)^{n,n+1}_{j+\frac12}-(\mathcal{F}_i)^{n,n+1}_{j-\frac12}}{\Delta x}\\ &-\beta\,\Delta t\begin{pmatrix}(\beta-1)\,\left(\Delta(\rho u^2)\right)^n_j + (2-\beta)\,\left(\Delta(\rho u^2)\right)^\star_j + \dfrac{(1-\beta)}{\varepsilon}\,(\Delta p(\rho))^\star_j + \dfrac{\beta}{\varepsilon}\,(\Delta p(\rho))^{n+1}_j\\ 0\end{pmatrix} = 0.\end{aligned} \tag{10b}$$

Lemma 1. *The scheme (9) is asymptotically consistent with system (2) in the limit $\varepsilon \to 0$.*

Proof. We do not assume well-prepared initial conditions but general initial conditions $\rho(0,x) = \rho^0(x)$ and $U(0,x) = U^0(x)$. Well-prepared initial conditions will also converge to a constant density and a divergence free velocity when ε tends to 0. We consider the boundary condition $U(x,t)\cdot\nu(x) = 0$ for all $t \geq 0$ and all $x \in \partial\Omega$, where $\partial\Omega$ is the boundary of Ω and where ν is the outward unit normal.

We assume that all discrete quantities (densities and momenta) have a limit when $\varepsilon \to 0$. At the first time-step $n = 0$, multiplying the momentum equation of (9a) and letting ε tend to 0 gives $\nabla p(\rho^\star) = 0$, and so $\nabla\rho^\star = 0$. Then, integrating the mass equation of (9a) on the domain and using the boundary condition $U^\star\cdot\nu = 0$ on $\partial\Omega$, one gets $\rho^\star =< \rho^0 >= 1/|\Omega|\int_\Omega \rho^0(x)\,dx$. Similarly, the second stage (9b) gives $\nabla\rho^1 = 0$, and integrating the mass equation as well as using the boundary conditions $U^\star\cdot\nu = U^1\cdot\nu = 0$ yields $\rho^1 = \rho^\star =< \rho^0 >$.

Note that inserting this result into the mass equation of the first stage (9a) does not recover the incompressibility constraint for the first time-step. Indeed, $\nabla\cdot U^\star(x) = (< \rho^0 > -\rho^0(x))/(\Delta t\ < \rho^0 >)$, which vanishes if and only if the initial density ρ^0 is well-prepared and tends to a constant value when ε tends to 0. But, for all $n \geq 1$, we recover the incompressibility constraint for the first stage $\nabla\cdot U^\star = 0$. Finally, thanks to $\nabla\cdot U^\star = 0$, the density equation gives $\nabla\cdot U^{n+1} = 0$ for all $n \geq 1$. Consequently, the scheme projects the solution over the asymptotic incompressible limit even if the initial data are not well-prepared to this limit: we obtain $\rho^{n+1} =< \rho^0 >:= \rho_0$ and $\nabla\cdot U^{n+1} = 0$ for all $n \geq 1$. Concerning the pressure, for $n \geq 1$, the limit scheme becomes

$$\rho_0\,\frac{U^\star - U^n}{\Delta t} + \beta\,\rho_0\nabla\cdot(U\otimes U)^n + \beta\,\nabla\pi_1^\star = 0, \tag{11a}$$

$$\rho_0\,\frac{U^{n+1}-U^n}{\Delta t} + (\beta-1)\,\rho_0\nabla\cdot(U\otimes U)^n + (2-\beta)\,\rho_0\nabla\cdot(U\otimes U)^\star + (1-\beta)\,\nabla\pi_1^\star + \beta\,\nabla\pi_1^{n+1} = 0, \tag{11b}$$

where $\pi_1^\star = \lim_{\varepsilon\to 0}\frac{1}{\varepsilon}\left(p(\rho^\star) - p(\rho_0)\right)$ and $\pi_1^{n+1} = \lim_{\varepsilon\to 0}\frac{1}{\varepsilon}\left(p(\rho^{n+1}) - p(\rho_0)\right)$. □

Remark 1. *Let us note that it is also possible to prove the consistency of the fully discretized scheme in one dimension and for periodic boundary conditions. The proof is similar to that done in [18] for a similar scheme. To be more precise, in the fully discrete case, one can prove that, if the approximate solution has a limit when ε tends to 0, then the limit density and momentum are constant in space and time, and they are given by the mean values (on the mesh) of the initial conditions.*

Now, we test this second-order accurate uncoupled AP scheme (10) on a 1D shock tube test case. The space domain is $[0,1]$ and we set $\gamma = 1.4$. The initial data is given by (29) and the CFL condition is uniform and given

by (8), and the space discretization is first-order accurate. The exact solution is made of a left rarefaction wave and a right shock wave. Figure 3 reports the numerical density ρ given by the first- and second-order AP schemes described above, with homogeneous Neumann boundary conditions. Note that we test these schemes for several values of the squared Mach number ε. For each value of ε, we take different final physical times t_{end} to make sure that the waves do not exit the computational domain. In addition, the number L of cells increases when ε decreases. This choice was made to highlight the differences between the schemes: too many cells for larger ε would make the numerical results look alike, while too few cells for smaller ε would result in too smeared an approximation.

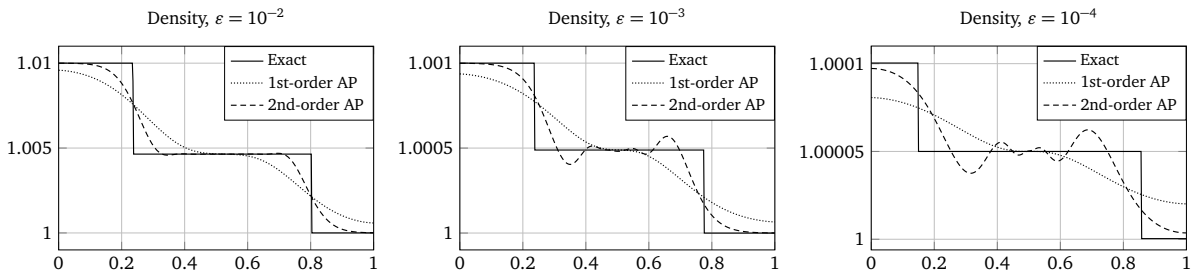

Figure 3: Density ρ as a function of space for a rarefaction-shock Riemann problem for the 1D isentropic Euler system (1) with initial data given by (29). For different values of ε, we compare the exact solution (solid line) to the first-order AP scheme (5) (dotted line) and the second-order AP scheme (10) (dashed line). The final physical time t_{end} and the number L of discretization cells are given by $t_{end} = 2 \times 10^{-2}$s and $L = 125$ for $\varepsilon = 10^{-2}$; $t_{end} = 6 \times 10^{-3}$s and $L = 250$ for $\varepsilon = 10^{-3}$; and $t_{end} = 2.5 \times 10^{-3}$s and $L = 500$ for $\varepsilon = 10^{-4}$.

As we can see, the second-order AP scheme gives more accurate results but it presents some oscillations when the Mach number decreases for a fixed value of the time step given by the CFL condition (8). These oscillations disappear when the time step is reduced and, in particular, when the non uniform explicit CFL condition is satisfied ($\Delta t \leq \Delta x/(\max_j \left(|u_j^n \pm \sqrt{p'(\rho_j^n)/\varepsilon}|\right)$). Thus, as expected, a second-order implicit-explicit time discretization for this kind of problem suffers from the same limitations as standard implicit time discretizations for hyperbolic problems of order higher than one: the TVD property is lost. In the forthcoming developments, we first study and find a solution to the above problematic situations in the simplified setting of a linear transport equation. Then, we extend the proposed technique to the case of the Euler equations.

4. Study of the stability on a model problem

We consider the linear advection equation:

$$\partial_t w + c_e \partial_x w + \frac{c_i}{\sqrt{\varepsilon}} \partial_x w = 0, \tag{12}$$

with $c_e > 0$ and $c_i > 0$ fixed real numbers. Note that the dependency in $\sqrt{\varepsilon}$ of the fast velocity is similar to that of the velocity of the pressure waves in the Euler system. The formal limit $\varepsilon \to 0$ of the above equation is a constant and uniform solution. The first-order AP scheme detailed in the previous section becomes

$$w_j^{n+1} = w_j^n - \frac{\Delta t}{\Delta x} c_e \left(w_j^n - w_{j-1}^n\right) - \frac{\Delta t}{\Delta x} \frac{c_i}{\sqrt{\varepsilon}} \left(w_j^{n+1} - w_{j-1}^{n+1}\right). \tag{13}$$

We recall that, in this particular one dimensional constant linear case, all schemes (upwind, Godunov, Lax-Friedrichs, Rusanov) give the same discretization. This is no longer true for linear systems or for nonlinear (even one dimensional) equations. The following result holds:

Lemma 2. *Prescribe periodic boundary conditions $w_0^n = w_L^n$ and $w_{L+1}^n = w_1^n$ for all $n \geq 0$ and assume that the following uniform CFL condition holds true*

$$\Delta t \leq \frac{\Delta x}{c_e}. \tag{14}$$

Then, the scheme (13) is asymptotic preserving and asymptotically L^2- and L^∞-stable, that is

$$\left\|w^{n+1}\right\|_2 = \left(\sum_{j=1}^{L} |w_j^{n+1}|^2\right)^{1/2} \leq \|w^n\|_2 \qquad \textit{and} \qquad \left\|w^{n+1}\right\|_\infty = \max_{j=1}^{L} |w_j^{n+1}| \leq \|w^n\|_\infty .$$

In addition, it is TVD, since

$$TV(w^{n+1}) \leq TV(w^n) = \sum_{j=1}^{L} \left|w_{j+1}^n - w_j^n\right|.$$

Proof. The proofs of the asymptotic consistency and of the L^2- and L^∞-stabilities can be easily established following the results proved in [22] and we omit them. It remains to prove the TVD property. Using (13) and the periodic boundary conditions, we have, for all $j \in \{1, \cdots, L\}$,

$$\left(w_{j+1}^{n+1} - w_j^{n+1}\right)\left(1 + \frac{c_i\,\Delta t}{\sqrt{\varepsilon}\,\Delta x}\right) - \frac{c_i\,\Delta t}{\sqrt{\varepsilon}\,\Delta x}\left(w_j^{n+1} - w_{j-1}^{n+1}\right) = \left(w_{j+1}^n - w_j^n\right)\left(1 - \frac{c_e\,\Delta t}{\Delta x}\right) + \frac{c_e\,\Delta t}{\Delta x}\left(w_j^n - w_{j-1}^n\right).$$

Recall that, for all real numbers a and b, we have $|a| - |b| \leq |a - b|$. Then, taking the absolute value of the above expression, summing for all $j \in \{1, \cdots, L\}$ and using the periodic boundary conditions and the CFL condition (14), we obtain

$$\begin{aligned}
\sum_{j=1}^{L} \left|w_{j+1}^{n+1} - w_j^{n+1}\right| &= \left(1 + \frac{c_i\,\Delta t}{\sqrt{\varepsilon}\,\Delta x}\right)\sum_{j=1}^{L} \left|w_{j+1}^{n+1} - w_j^{n+1}\right| - \frac{c_i\,\Delta t}{\sqrt{\varepsilon}\,\Delta x}\sum_{j=1}^{L} \left|w_j^{n+1} - w_{j-1}^{n+1}\right| \\
&\leq \sum_{j=1}^{L}\left(1 + \frac{c_i\,\Delta t}{\sqrt{\varepsilon}\,\Delta x}\right)\left|\left(w_{j+1}^{n+1} - w_j^{n+1}\right) - \frac{c_i\,\Delta t}{\sqrt{\varepsilon}\,\Delta x}\left(w_j^{n+1} - w_{j-1}^{n+1}\right)\right| \\
&\leq \left(1 - \frac{c_e\,\Delta t}{\Delta x}\right)\sum_{j=1}^{L} \left|w_{j+1}^n - w_j^n\right| + \frac{c_e\,\Delta t}{\Delta x}\sum_{j=1}^{L} \left|w_j^n - w_{j-1}^n\right| = \sum_{j=1}^{L} \left|w_{j+1}^n - w_j^n\right|.
\end{aligned}$$

The proof is thus achieved. □

We turn now our attention to the two-step ARS(2,2,2) second-order time discretization; we refer to it to as second-order AP scheme. This reads

$$w_j^\star = w_j^n - \beta c_e \frac{\Delta t}{\Delta x}\left(w_j^n - w_{j-1}^n\right) - \beta \frac{c_i}{\sqrt{\varepsilon}}\frac{\Delta t}{\Delta x}\left(w_j^\star - w_{j-1}^\star\right), \tag{15a}$$

$$\begin{aligned}
w_j^{n+1} = w_j^n &- (\beta - 1)c_e \frac{\Delta t}{\Delta x}\left(w_j^n - w_{j-1}^n\right) - (1 - \beta)\frac{c_i}{\sqrt{\varepsilon}}\frac{\Delta t}{\Delta x}\left(w_j^\star - w_{j-1}^\star\right) \\
&- (2 - \beta)c_e \frac{\Delta t}{\Delta x}\left(w_j^\star - w_{j-1}^\star\right) - \beta \frac{c_i}{\sqrt{\varepsilon}}\frac{\Delta t}{\Delta x}\left(w_j^{n+1} - w_{j-1}^{n+1}\right).
\end{aligned} \tag{15b}$$

Proposition 1. *For periodic boundary conditions, the two-step scheme (15) is asymptotically consistent: if $w_j^0 = \overline{w}$ for all $j \in \{1, \cdots, L\}$, then for all $n \geq 0$, $w_j^n = \overline{w}$, for all $j \in \{1, \cdots, L\}$.*

Proof. Multiplying both equations of (15) by $\sqrt{\varepsilon}$ and passing to the limit $\varepsilon \to 0$ yields $w_j^\star = w_1^\star$ and $w_j^{n+1} = w_1^{n+1}$ for all $j \in \{1, \cdots, L\}$. Now summing (15b) for $j \in \{1, \cdots, L\}$, we obtain by induction $w_j^{n+1} = w_1^{n+1} = w_1^n = \cdots = \overline{w}$. □

Concerning the L^2-stability of the scheme (15), we can prove the following result:

Proposition 2. *For periodic boundary conditions, the scheme (15) is L^2-stable under the CFL condition (14).*

Proof. Using Fourier analysis and setting $w_j^{n+1,\star,n} = \sum_k \hat{w}_k^{n+1,\star,n}\, e^{i\,k\,j\,\Delta x}$, we obtain that $w_k^\star = f_k\, w_k^n$ and $w_k^{n+1} = g_k\, w_k^n$, where $f_k = (1-\beta\,\sigma_e\,(1-c+i\,s))/(1+\beta\,\sigma_i^\varepsilon\,(1-c+i\,s))$ with $\sigma_e = \frac{c_e\,\Delta t}{\Delta x}$, $\sigma_i^\varepsilon = \frac{c_i\,\Delta t}{\varepsilon\,\Delta x}$, $c = \cos(k\,\Delta x)$, $s = \sin(k\,\Delta x)$, and where

$$g_k = \frac{1-(\beta-1)\,\sigma_e\,(1-c+i\,s)}{1+\beta\,\sigma_i^\varepsilon\,(1-c+i\,s)} - \frac{\Big((1-\beta)\,\sigma_i^\varepsilon + (2-\beta)\sigma_e\Big)(1-c+i\,s)\;(1-\beta\,\sigma_e\,(1-c+i\,s))}{(1+\beta\,\sigma_i^\varepsilon\,(1-c+i\,s))^2}.$$

Remarking that $x\,(1-x) \in [0,1/4]$ for all $x \in [0,1]$, we easily obtain that, under the condition $\beta\,\sigma_e = \beta\,\frac{c_e\,\Delta t}{\Delta x} \leq 1$, we have $|f_k|^2 \leq 1 - 2\,(\beta\sigma_e)\,(1-c)\,(1-2\,\beta\,\sigma_e) \leq 1$, for all $\sigma_i^\varepsilon \geq 0$ and $c \in [-1,1]$. Furthermore, an easy calculation shows that $|g_k|^2$ depends only on s^2 and has a finite limit when $\sigma_i^\varepsilon \to +\infty$. Then, setting $\sigma_e = 1$ to plot the function $(c,\sigma_i^\varepsilon) \mapsto |g_k|^2$ for $c \in [-1,1]$ and $\sigma_i^\varepsilon \in [0,1]$, and setting $\sigma_e = 1$, $\mu_i^\varepsilon = 1/\sigma_i^\varepsilon$ to plot the function$(c,\mu_i^\varepsilon) \mapsto |g_k|^2$ for $c \in [-1,1]$ and $\mu_i^\varepsilon \in [0,1]$, we prove that, for all $\sigma_i^\varepsilon \geq 0$ and $c \in [-1,1]$,

$$\sigma_e = \frac{c_e\,\Delta t}{\Delta x} \leq 1 \quad \Rightarrow \quad |g_k|^2 \leq 1.$$

The scheme (15) is therefore L^2-stable under the uniform CFL condition (14), and the proof is concluded. □

However, the above scheme is neither uniformly L^∞-stable nor uniformly TVD under the non-restrictive CFL condition (14). Let us show it with a counterexample. We take $c_e = c_i = 1$, and we consider the following initial data on the space domain $[0,1]$:

$$w(0,x) = \begin{cases} \sqrt{\varepsilon} & \text{if } 0 \leq x < 0.5, \\ -\sqrt{\varepsilon} & \text{otherwise.} \end{cases} \tag{16}$$

and on Figure 4, we display the results of the first-order AP scheme (13) and the second-order AP scheme (15) for two different values of the Mach number using the non-restrictive CFL condition (14) and periodic boundary conditions. The final physical time is chosen with respect to ε, and we take $t_{end} = 0.4\,(c_e + c_i/\sqrt{\varepsilon})$. The results are the following: the first-order AP scheme is in-bounds but diffusive, the second-order AP scheme produces bounded spurious oscillations when the time step violates the explicit CFL condition $\Delta x/(c_e + c_i/\sqrt{\varepsilon})$, thus preventing it from being L^∞-stable or TVD independently of ε.

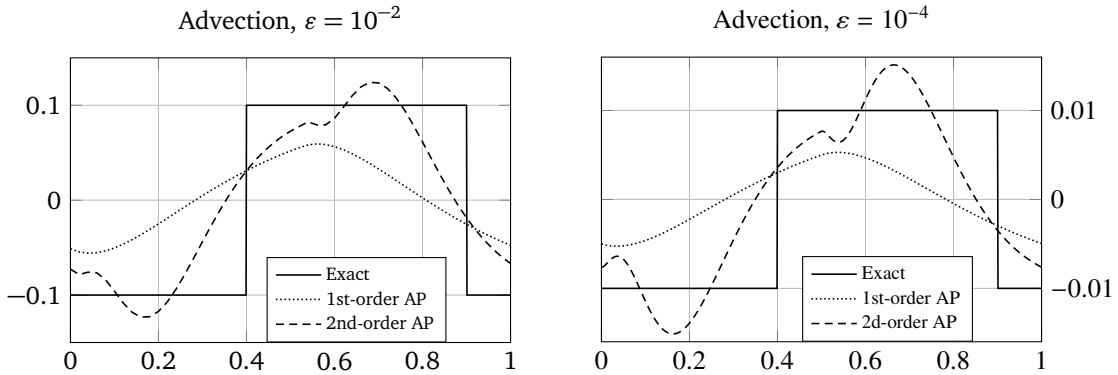

Figure 4: Advection with equation (12) of the rectangular pulse (16). Comparison of the first-order AP scheme (13) (dotted line) and the second-order AP scheme (15) (dashed line) against the exact solution (solid line). We set $c_e = c_i = 1$ and $t_{end} = 0.4\,(c_e + c_i/\sqrt{\varepsilon})$. In the left panel, we take $\varepsilon = 10^{-2}$ and 50 discretization cells; in the right panel, we take $\varepsilon = 10^{-4}$ and 500 discretization cells.

This loss of stability for the case of an implicit-explicit second-order scheme shares many similarities with a negative result [30] proved in the case of sole implicit high-order Runge-Kutta time discretizations that we recall here:

Theorem 1. *([30]) There do not exist TVD implicit Runge-Kutta discretizations of order higher than one with unconstrained time steps.*

We wish to tackle this problem and to obtain a TVD numerical scheme that is more accurate than a first-order discretization. To that end, we propose to introduce a convex combination between a first-order implicit-explicit scheme and the IMEX ARS discretization, as follows:

$$w_j^{n+1} = \theta\, w_j^{n+1,O1} + (1-\theta)\, w_j^{n+1,O2},$$

where $w_j^{n+1,O1}$ is given by the first-order AP scheme (13), $w_j^{n+1,O2}$ by the second-order AP one (15), and where $\theta \in [0,1]$. The spirit is the same as high-resolution methods employing the so-called flux limiter approach [47] for constructing high-order TVD schemes. Since, as in the case of high-order space discretizations, it is not possible to avoid spurious oscillations, we couple high-order discretizations with first-order ones. In cases where the TVD property is violated, we come back to the first-order discretization which ensures monotonicity. This approach gives the following limited scheme:

$$w_j^\star = w_j^n - \beta c_e \frac{\Delta t}{\Delta x}\left(w_j^n - w_{j-1}^n\right) - \beta \frac{c_i}{\sqrt{\varepsilon}} \frac{\Delta t}{\Delta x}\left(w_j^\star - w_{j-1}^\star\right), \tag{17a}$$

$$\begin{aligned} w_j^{n+1} = w_j^n &- \theta(\beta-1) c_e \frac{\Delta t}{\Delta x}\left(w_j^n - w_{j-1}^n\right) - \theta(1-\beta)\frac{c_i}{\sqrt{\varepsilon}}\frac{\Delta t}{\Delta x}\left(w_j^\star - w_{j-1}^\star\right) \\ &- \theta(2-\beta) c_e \frac{\Delta t}{\Delta x}\left(w_j^\star - w_{j-1}^\star\right) - \theta\beta \frac{c_i}{\sqrt{\varepsilon}}\frac{\Delta t}{\Delta x}\left(w_j^{n+1} - w_{j-1}^{n+1}\right) \\ &- (1-\theta) c_e \frac{\Delta t}{\Delta x}\left(w_j^n - w_{j-1}^n\right) - (1-\theta)\frac{c_i}{\sqrt{\varepsilon}}\frac{\Delta t}{\Delta x}\left(w_j^{n+1} - w_{j-1}^{n+1}\right). \end{aligned} \tag{17b}$$

For this limited scheme (17), the following results hold true:

Theorem 2. *With periodic boundary conditions, the scheme (17) is asymptotically consistent.*

Proof. The scheme (17) results from a convex combination of the two asymptotically consistent schemes (13) and (15). Therefore, it is also asymptotically consistent. □

Theorem 3. *The scheme* (17) *is asymptotically stable, i.e. uniformly TVD and L^∞-stable:*

$$\left\|w^\star\right\|_\infty \le \|w^n\|_\infty, \qquad \left\|w^{n+1}\right\|_\infty \le \|w^n\|_\infty, \qquad TV(w^\star) \le TV(w^n), \qquad TV(w^{n+1}) \le TV(w^n),$$

if the following uniform CFL conditions

$$(1-\alpha)\,\frac{c_e\,\Delta t}{\Delta x} \le 1-\alpha, \qquad \alpha\,\frac{c_e\,\Delta t}{\Delta x} \le \alpha\,\frac{1}{\frac{\beta}{1-\beta}(2-\beta)} = \alpha\,\sqrt{2}, \tag{18}$$

are verified for $\alpha \in [0,1]$ and $\theta = \alpha\,\frac{\beta}{1-\beta} = \alpha\,(\sqrt{2}-1) \in (0,1)$.

Proof. Let us first note that, like for the first-order AP scheme, the first step (17a) of the scheme is TVD and L^∞-stable under the non-restrictive explicit CFL condition $c_e\,\Delta t/\Delta x \le 1/\beta$. This restriction automatically holds since $1 \le \sqrt{2} \le 1/\beta$. Therefore, $\left\|w^\star\right\|_\infty \le \|w^n\|_\infty$ and $TV\,(w^\star) \le TV\,(w^n)$.

Now, let us prove the L^∞-stability of the second step. We denote by j_0 the index in $\{1,\cdots,L\}$ such that $w_{j_0}^{n+1} = \max_{j=1}^{L} w_j^{n+1}$. Thanks to the periodic boundary conditions, we have $w_{j_0}^{n+1} = \max_{j=0}^{L+1} w_j^{n+1}$. Then, we rewrite the second step (17b) as follows:

$$\begin{aligned} w_{j_0}^{n+1} \le w_{j_0}^{n+1} + (1-\theta+\theta\beta)\,\frac{c_i\,\Delta t}{\sqrt{\varepsilon}\,\Delta x}(w_{j_0}^{n+1} - w_{j_0-1}^{n+1}) &= \left(1 - \theta(\beta-1)\frac{c_e\,\Delta t}{\Delta x} - (1-\theta)\frac{c_e\,\Delta t}{\Delta x}\right) w_{j_0}^n \\ &+ \left(\theta(\beta-1)\frac{c_e\,\Delta t}{\Delta x} + (1-\theta)\frac{c_e\,\Delta t}{\Delta x}\right) w_{j_0-1}^n \\ &- \theta(1-\beta)\frac{c_i\,\Delta t}{\sqrt{\varepsilon}\,\Delta x}(w_{j_0}^\star - w_{j_0-1}^\star) - \theta(2-\beta)\frac{c_e\,\Delta t}{\Delta x}(w_{j_0}^\star - w_{j_0-1}^\star). \end{aligned}$$

From the first step (17a), we deduce $-\frac{c_i\,\Delta t}{\sqrt{\varepsilon}}(w^\star_{j_0}-w^\star_{j_0-1})=\frac{1}{\beta}(w^\star_{j_0}-w^n_{j_0})+\frac{c_e\,\Delta t}{\Delta x}(w^n_{j_0}-w^n_{j_0-1})$. Plugging this expression into the previous equality leads to:

$$\max_{j=0}^{L+1} w_j^{n+1}=w_{j_0}^{n+1}\leq\left(1-\theta\,\frac{1-\beta}{\beta}-\frac{c_e\,\Delta t}{\Delta x}\Big(1-\theta\,\overbrace{(3-2\beta)}^{=(1-\beta)/\beta}\Big)\right)w^n_{j_0}+\frac{c_e\,\Delta t}{\Delta x}\left(1-\theta\,\frac{1-\beta}{\beta}\right)w^n_{j_0-1}$$
$$+\left(\theta\frac{1-\beta}{\beta}-\theta(2-\beta)\frac{c_e\,\Delta t}{\Delta x}\right)w^\star_{j_0}+\theta(2-\beta)\frac{c_e\,\Delta t}{\Delta x}w^\star_{j_0-1}.$$

Note that, if all the coefficients are positive, we will have two convex combinations, one at time index n and one at time index $\star$, and

$$\max_{j=0}^{L+1} w_j^{n+1}=w_{j_0}^{n+1}\leq\left(1-\theta\,\frac{1-\beta}{\beta}\right)\max_{j=0}^{L+1} w_j^n+\theta\,\frac{1-\beta}{\beta}\max_{j=0}^{L+1} w_j^\star\leq\max_{j=0}^{L+1} w_j^n.$$

From the above expression, we deduce that necessary conditions for positive coefficients are $1-\theta\,\frac{1-\beta}{\beta}\geq 0$ and $\theta\frac{1-\beta}{\beta}\geq 0$. This gives the condition $\theta\in[0,\beta/(1-\beta)]$. By setting $\theta=\alpha\,\frac{\beta}{1-\beta}$, with $\alpha\in[0,1]$, then all coefficients are positive under the CFL conditions (18) and consequently the L^∞-stability property is verified.

We can now prove the TVD property. Using (17b), the periodic boundary conditions and the first step, we have for all $j\in\{1,\cdots,L\}$:

$$\left(w^{n+1}_{j+1}-w^{n+1}_j\right)\left(1+(1-\theta+\theta\beta)\,\frac{c_i\,\Delta t}{\sqrt{\varepsilon}\,\Delta x}\right)-(1-\theta+\theta\beta)\,\frac{c_i\,\Delta t}{\sqrt{\varepsilon}\,\Delta x}\left(w^n_j-w^n_{j-1}\right)$$
$$=\left(w^n_{j+1}-w^n_j\right)\left(1-\theta\,\frac{1-\beta}{\beta}-\frac{c_e\,\Delta t}{\Delta x}\big(1+\theta\,(1-2\beta)\big)\right)+\left(w^n_j-w^n_{j-1}\right)\frac{c_e\,\Delta t}{\Delta x}\big(1+\theta\,(1-2\beta)\big)$$
$$+\left(w^\star_{j+1}-w^\star_j\right)\left(\theta\frac{1-\beta}{\beta}-\theta(2-\beta)\frac{c_e\,\Delta t}{\Delta x}\right)+\left(w^\star_j-w^\star_{j-1}\right)\theta(2-\beta)\frac{c_e\,\Delta t}{\Delta x}.$$

Taking the absolute value, remarking that for all real numbers a and b, $|a|-|b|\leq|a-b|$, summing for all $j\in\{1,\cdots,L\}$ and using the CFL conditions (18) and the periodic boundary conditions, we conclude the proof:

$$\sum_{j=1}^{L}|w^{n+1}_{j+1}-w^{n+1}_j|\leq\sum_{j=1}^{L}|w^n_{j+1}-w^n_j|\left(1-\theta\,\frac{1-\beta}{\beta}-\frac{c_e\,\Delta t}{\Delta x}\big(1+\theta\,(1-2\beta)\big)\right)+\sum_{j=1}^{L}|w^n_j-w^n_{j-1}|\,\frac{c_e\,\Delta t}{\Delta x}\big(1+\theta\,(1-2\beta)\big)$$
$$+\sum_{j=1}^{L}|w^\star_{j+1}-w^\star_j|\left(\theta\frac{1-\beta}{\beta}-\theta(2-\beta)\frac{c_e\,\Delta t}{\Delta x}\right)+\sum_{j=1}^{L}|w^\star_j-w^\star_{j-1}|\theta(2-\beta)\frac{c_e\,\Delta t}{\Delta x}\leq\sum_{j=1}^{L}|w^n_{j+1}-w^n_j|.$$

The scheme (17) is therefore asymptotically stable under the uniform CFL conditions (18). □

Remark 2. 1. *Theorem 3 shows that the largest possible value for θ is $\theta_M=\beta/(1-\beta)=\sqrt{2}-1\approx 0.4142$ to make sure that the TVD property and the L^∞-stability hold. The scheme* (17) *with $\theta=\theta_M$ will be referred to as the TVD-AP scheme. This value θ_M depends on the chosen second-order time discretization . Other time discretizations may allow larger values which may possibly improve the accuracy of the method. This situation will be discussed in detail in [51].*

2. *In order to further increase the accuracy of the method, one could introduce local values of θ, to get a different θ for each spatial cell in equation* (17)*. However, in this case, the proofs of the TVD property and the L^∞ stability remain an open problem. In addition, numerical experiments performed suggest that such a local parameter must be chosen related to a stencil of neighbors proportional to the velocity $c_i/\sqrt{\varepsilon}$. These aspects will be studied in detail in [51].*

Now, we discuss limiters to detect the situations in which the TVD or the L^∞ stability property is violated. In such situations, it is relevant to switch from the second-order accurate scheme to the TVD-AP scheme without losing excessive accuracy by diminishing the parameter θ. The proposed approach is based on a detection technique borrowed

from the MOOD (Multidimensional Optimal Order Detection) [12, 25, 26] framework. The idea behind this specific MOOD approach is to use the second-order oscillatory discretization (15) whenever possible, i.e. when no oscillations appear. Instead, if at time n the numerical solution presents oscillations, we discard it and we replace it by the limited TVD-AP scheme, i.e. the scheme (17) with $\theta = \theta_M = \beta/(1-\beta)$, which ensures the preservation of the demanded properties. Since, for this specific situation, the L^∞ norm of the solution is preserved in time, spurious oscillations are checked with respect to the initial condition instead of that of the previous time iteration of the scheme. Indeed, the relevant bounds are those of the initial condition rather than the ones of the diffusive numerical approximation. The procedure is summarized by the following algorithm:

Algorithm 1.
1. *Compute a candidate solution $w^{n+1,O2}$ using the second-order AP scheme (15).*
2. *Detect if this candidate solution satisfies the L^∞-stability and the TVD properties.*
3. *If these two criteria are satisfied by $w^{n+1,O2}$, set $w^{n+1} = w^{n+1,O2}$; otherwise, compute w^{n+1} using the TVD-AP scheme (17) with $\theta = \theta_M = \beta/(1-\beta)$.*

When this Algorithm is used, the resulting scheme will be referred to as the AP-MOOD scheme. In Figure 5, we report the results of the advection of the rectangular pulse given by (16), for different values of the parameter ε, and with periodic boundary conditions. Once again, we take $c_e = c_i = 1$, and the final physical time is $t_{end} = 0.4\,(c_e + c_i/\sqrt{\varepsilon})$. The solution is computed by the first-order AP scheme, the second-order AP scheme, the TVD-AP scheme and the AP-MOOD scheme. The exact solution is also reported. One can clearly see the differences in terms of accuracy for the different methods proposed and the absence of spurious oscillations for the TVD-AP and the AP-MOOD methods. In the next section, we extend this approach to the case of the Euler equations.

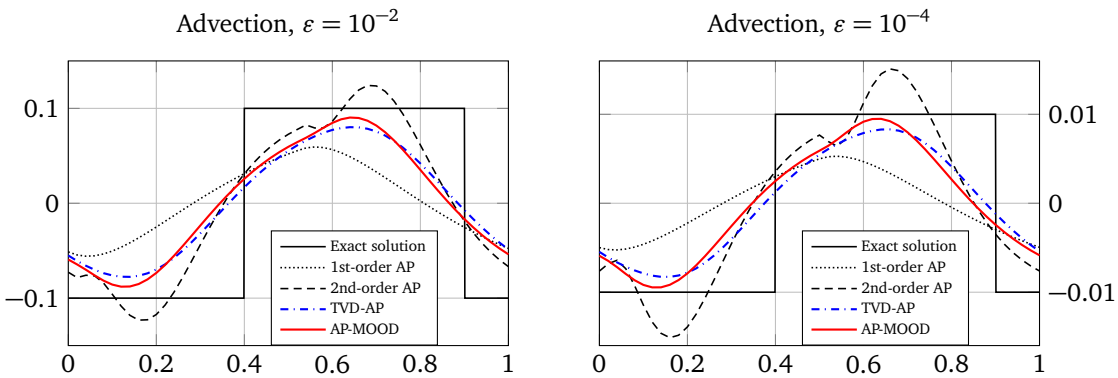

Figure 5: Advection with equation (12) of the rectangular pulse (16). Comparison of the first-order AP scheme (13) (dotted line), the second-order AP scheme (15) (dashed line) the TVD-AP scheme (17) (blue dash-dotted line) and of AP-MOOD scheme given by Algorithm 1 (red line) against the exact solution (solid line). We set $c_e = c_i = 1$ and $t_{end} = 0.4\,(c_e + c_i/\sqrt{\varepsilon})$. In the left panel, we take $\varepsilon = 10^{-2}$ and 50 discretization cells; in the right panel, we take $\varepsilon = 10^{-4}$ and 500 discretization cells.

5. Application to the isentropic Euler system

We now extend the idea developed in the previous section to the isentropic Euler system. The TVD-AP scheme reads as follows:

$$W_j^{n+1} = \theta\, W_j^{n+1,O1} + (1-\theta)\, W_j^{n+1,O2}, \tag{19}$$

where $W_j^{n+1,O1}$ is given by the first-order AP scheme (5) while $W_j^{n+1,O2}$ is given by the second-order AP scheme (10). The value of θ comes from the analysis of the model problem carried out in the previous section: we set θ equal to the fixed value $\theta_M = \beta/(1-\beta)$. This is enough to ensure the TVD and the L^∞-stability properties. However, we observed that in many situations the full second-order AP scheme (10) can be employed without formation of spurious oscillations like in the linear advection case described before. Our goal is therefore to construct a MOOD-like technique which allows an interpolation from the full second-order to the TVD-AP scheme if needed. This will

produce *de facto* an highly accurate method which is referred to as the AP-MOOD method. Unfortunately, in this case, one cannot directly transpose to the Euler case the MOOD approach seen for the advection equation. In fact, in the Euler system, the variables ρ and ρu no longer satisfy either the TVD property or the L^∞ bound in the continuous case. As a consequence, we cannot apply the detection criteria seen before on the conservative variables ρ and ρu to get a non oscillating scheme. It turns out that characteristic or Riemann invariants variables constitute a better choice for detecting spurious oscillations since it can be shown that they verify some decoupled non linear advection equations [69]. We denote the Riemann invariants by ϕ_+ and ϕ_-. For the isentropic Euler system case, they are given by

$$\phi_+(W) := u - h(\rho), \qquad \text{and} \qquad \phi_-(W) := u + h(\rho), \tag{20}$$

where $h(\rho)$ is the enthalpy given by $h(\rho) = \frac{2}{\gamma-1}\sqrt{\frac{\gamma\rho^{\gamma-1}}{\varepsilon}}$ if $\gamma > 1$ and $h(\rho) = \ln(\rho)$ if $\gamma = 1$ (see [69]). Note that, after [67], it is known that at continuous level and for a Riemann problem at least one of the two Riemann invariants ϕ_+ or ϕ_- satisfy the maximum principle. Therefore, one can think to introduce a MOOD-like detection criterion which relies on testing whether both Riemann invariants break the maximum principle at the same time. In practice, the following stability detector is used:

$$\begin{cases} M_\pm^0 = \|\phi_\pm^0\|_\infty, \\ M_\pm^n = \max\left(M_\pm^{n-1}, \|\phi_\pm^n\|_\infty\right), \text{ for all } n > 0. \end{cases}$$

Equipped with this detector, the AP-MOOD algorithm for the Euler equations reads as follows:

Algorithm 2. 1. *Compute a candidate solution $W^{n+1,O2}$ using the second-order AP scheme (10).*
2. *Detect if this candidate solution satisfies the maximum principle of the Riemann invariants: $\|\phi_-^{n+1,O2}\|_\infty \leq M_-^n$ and $\|\phi_+^{n+1,02}\|_\infty \leq M_+^n$.*
3. *If these two criteria are satisfied, set $W^{n+1} = W^{n+1,O2}$. Otherwise, compute W^{n+1} using the TVD-AP scheme (19).*

With this approach, at most one extra computation of the semi-implicit scheme is required to ensure the TVD property and the L^∞-stability.

We now turn to a second-order discretization in space. We present it in the case of one space dimension for the sake of simplicity. To this end, we use classical MUSCL techniques [70]; other high-order space reconstructions could also be employed without changing the core of the method. The discretization under consideration works by introducing a linear reconstruction of the conserved variables W_j^n:

$$\widehat{W}_j^n(x) = W_j^n + \sigma_j^n(x - x_j), \tag{21}$$

where σ_j^n can be a limited (if the TVD property should be ensured) or unlimited slope. On the one hand, the case of an unlimited slope is used in combination with the second-order in time AP scheme (10) and it is given by

$$\sigma_j^n = \frac{1}{2}\left(\frac{W_j^n - W_{j-1}^n}{\Delta x} + \frac{W_{j+1}^n - W_j^n}{\Delta x}\right). \tag{22}$$

This gives rise to a genuine second-order in time and space asymptotic preserving method which, however, does not enjoy either the TVD property or the L^∞-stability. On the other hand, the slope limited by the minmod limiter is employed together with AP-TVD scheme in time (19). In this case, we have

$$\sigma_j^n = \text{minmod}\left(\frac{W_j^n - W_{j-1}^n}{\Delta x}, \frac{W_{j+1}^n - W_j^n}{\Delta x}\right), \tag{23}$$

where the minmod function is given by:

$$\text{minmod}(a, b) = \begin{cases} \min(a, b) & \text{if } a > 0 \text{ and } b > 0, \\ \max(a, b) & \text{if } a < 0 \text{ and } b < 0, \\ 0 & \text{otherwise.} \end{cases}$$

The above combination of space and time discretization gives rise to a TVD-A highly accurate space and time discretization of the Euler equation.

The reconstruction (21) of the conserved variables W is evaluated at the inner interfaces as follows:

$$W^n_{j,\pm} := \widehat{W}^n_j\left(x_j \pm \frac{\Delta x}{2}\right) = W^n_j \pm \frac{\Delta x}{2}\sigma^n_j. \tag{24}$$

Thus, the explicit numerical flux function $\mathcal{F}_e$ becomes

$$(\mathcal{F}_e)^n_{j+\frac{1}{2}} := \frac{F_e(W^n_{j,+}) + F_e(W^n_{j+1,-})}{2} + (\mathcal{D}_e)^n_{j+\frac{1}{2}}(W^n_{j+1,-} - W^n_{j,+}), \tag{25}$$

with $(\mathcal{D}_e)^n_{j+\frac{1}{2}} := \max\left(|u^n_{j,+}|, |u^n_{j+1,-}|\right)$ the explicit viscosity coefficient. Moreover, the implicit numerical flux function $\mathcal{F}_i$ becomes

$$(\mathcal{F}_i)^{n,n+1}_{j+\frac{1}{2}} := \frac{F_i(W^{n,n+1}_{j,+}) + F_i(W^{n,n+1}_{j+1,-})}{2} + (\mathcal{D}_i)^n_{j+\frac{1}{2}}(\widetilde{W}^{n+1}_{j+1,-} - \widetilde{W}^{n+1}_{j,+}), \tag{26}$$

where $W^{n,n+1}_{j,+} = (\rho^{n+1}_{j,+}, (\rho u)^n_{j,+})$, where $(\mathcal{D}_i)^n_{j+\frac{1}{2}}$ is the implicit viscosity coefficient, taken as half of the maximum implicit eigenvalue and given by

$$(\mathcal{D}_i)^n_{j+\frac{1}{2}} := \frac{1}{2}\max\left(\sqrt{\frac{p'(\rho^n_{j,+})}{\varepsilon}}, \sqrt{\frac{p'(\rho^n_{j+1,-})}{\varepsilon}}\right), \tag{27}$$

and where we have set

$$\widetilde{W}^{n+1}_{j,\pm} = W^{n+1}_j \pm \frac{\Delta x}{2}\sigma^n_j. \tag{28}$$

The second-order MUSCL extension in space is thus completely defined.

6. Numerical experiments

The schemes described in the previous parts are resumed and labeled below.

- The first-order AP scheme is given by (5), (6) and (7).
- The second-order AP scheme is given by (10), (22), (24)-(28). It corresponds to the unlimited ARS(2,2,2) time discretization, supplemented with the unlimited linear MUSCL space reconstruction.
- The second-order limited AP scheme is given by (10), (23), (24)-(28). It corresponds to the unlimited ARS(2,2,2) time discretization, supplemented with the minmod limited linear MUSCL space reconstruction.
- The TVD-AP scheme is given by (19) with $\theta = \beta/(1-\beta)$. It corresponds to the convex combination of the first-order AP scheme and of the second-order limited AP scheme.
- The AP-MOOD scheme corresponds to the procedure detailed in Algorithm 2 with (25), (26) and limiter (23) for the space discretization.

In addition, for all the schemes, the time step is constrained by the uniform CFL condition

$$\Delta t \leq C\frac{\Delta x}{\Lambda}, \qquad \text{where } \Lambda = \max_j\left(2\,|u^n_j|\right),$$

with $C = 0.9$ for the first-order scheme and $C = 0.45$ for the other three schemes. Note that this slightly more restrictive CFL condition (for the second-order AP, TVD-AP and AP-MOOD schemes) is uniform and is only due to the second-order discretization in space. In the following, we first consider a one dimensional Riemann problem. Then, we perform an assessment of the order of accuracy of the scheme using a smooth solution in one space dimension. Afterwards, we validate the scheme on a more complex test case and we verify its asymptotic stability, again in one space dimension. Finally, we propose two two-dimensional numerical experiments to once again test the order of accuracy of the four schemes and to compare their results with a reference solution.

6.1. One-dimensional shock tube

On the space domain $[0, 1]$, we consider $\gamma = 1.4$ and a Riemann problem for the 1D isentropic Euler equations (1) with the following initial data:

$$\rho(0, x) = \begin{cases} 1 + \varepsilon & \text{if } x < 0.5, \\ 1 & \text{otherwise;} \end{cases} \qquad (\rho u)(0, x) = 1. \tag{29}$$

Homogeneous Neumann boundary conditions are prescribed on each boundary. The exact solution of this Riemann problem is made of a left rarefaction wave and a right shock wave. We compare the results from the three schemes in several regimes corresponding to different values of the squared Mach number: $\varepsilon = 1$, $\varepsilon = 10^{-2}$ and $\varepsilon = 10^{-4}$. For each value of ε, we take a different number L of discretization cells. This is due to the fact that, for ε close to 1, a large number of spatial cells would render the four different approximations very close and almost indistinguishable. On the other hand, a low number of cells for ε close to 0 would make every scheme too diffusive and any relevant conclusion would be impossible to draw. The results are displayed in Figure 6 for $\varepsilon = 1$ and $L = 50$, in Figure 7 for $\varepsilon = 10^{-2}$ and $L = 125$ and in Figure 8 for $\varepsilon = 10^{-4}$ and $L = 500$; the density is displayed on the left while the momentum is displayed on the right.

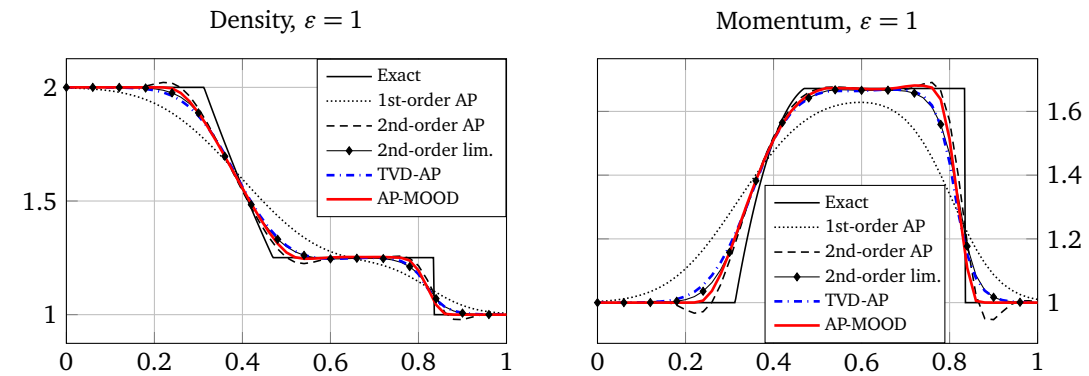

Figure 6: Comparison of the schemes for a one-dimensional shock tube for the 1D isentropic Euler system (1) with the initial conditions (29). We take $\varepsilon = 1$ and 50 discretization cells; the results are displayed as functions of space at time $t_{end} = 0.125$s. The left panel shows the density ρ while the right panel displays the momentum ρu.

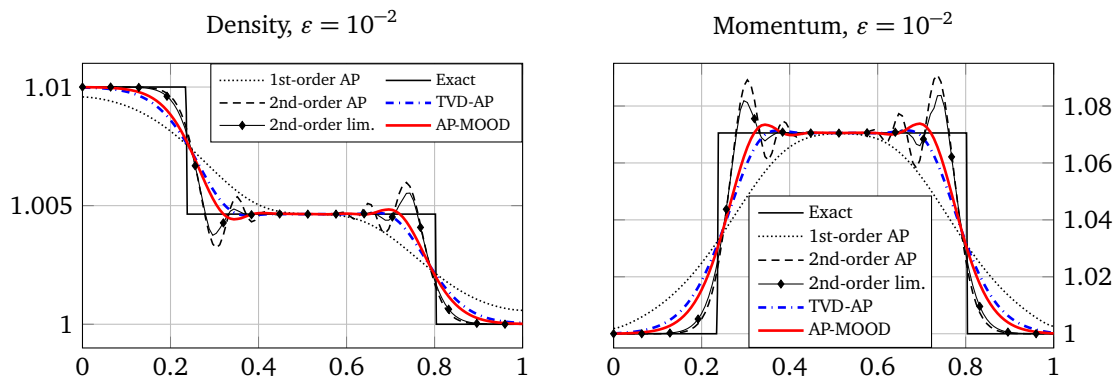

Figure 7: Comparison of the schemes for a one-dimensional shock tube for the 1D isentropic Euler system (1) with the initial conditions (29). We take $\varepsilon = 10^{-2}$ and 125 discretization cells; the results are displayed as functions of space at time $t_{end} = 2 \times 10^{-2}$s. The left panel shows the density ρ while the right panel displays the momentum ρu.

As expected, the first-order AP scheme (dotted line) is very diffusive, while the second-order scheme (dashed line) yields a better approximation of the intermediate states. However, overshoots and undershoots appear at the head

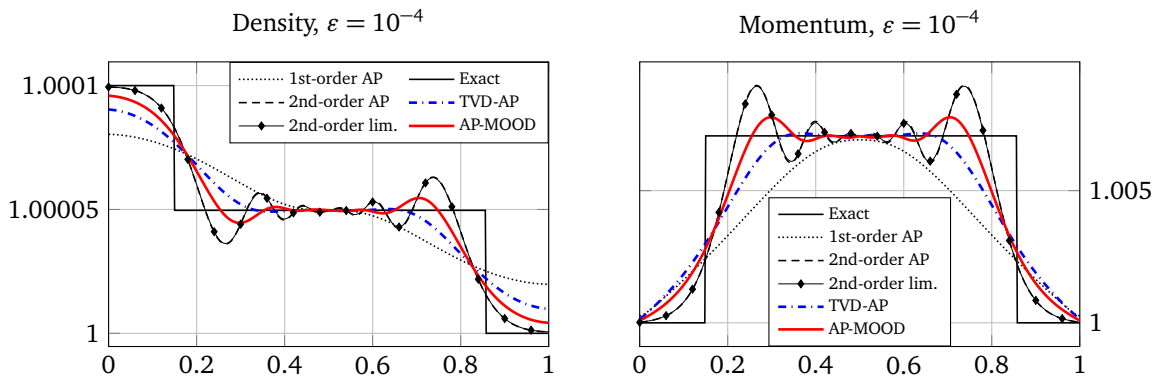

Figure 8: Comparison of the schemes for a one-dimensional shock tube for the 1D isentropic Euler system (1) with the initial conditions (29). We take $\varepsilon = 10^{-4}$ and 500 discretization cells; the results are displayed as functions of space at time $t_{end} = 2.5 \times 10^{-3}$s. The left panel shows the density ρ while the right panel displays the momentum ρu.

and tail of the rarefaction wave and near the shock wave. The TVD-AP scheme (blue line) corrects both of these shortcomings. Finally, thanks to the MOOD procedure, the AP-MOOD scheme (blue dashed line) yields better results than the TVD-AP scheme.

In addition, it is worth noting that the time limiter (i.e. the convex combination procedure) has little impact for ε close to one: in fact the TVD-AP scheme (blue line) and the second-order limited scheme (solid line with diamond marks) are very close on Figure 6. This is expected since, in this situation, the time step is the one of the explicit method, which means that the SSP property is guaranteed by the high-order time discretization. Conversely, for ε close to zero, the second-order limited scheme in space (solid line with diamond marks) is very close to the one produced by the unlimited version (dashed line) on Figures 7 and 8. This means that the space limiter of the standard TVD method is not able to remove the oscillations. The numerical oscillations are produced by the time discretization and a limiter for this part of the scheme is indeed necessary.

In conclusion, the oscillatory nature of the second-order AP scheme is removed by the TVD-AP and AP-MOOD schemes at the cost of an expected slightly increased diffusion. Moreover, regarding the quality of the numerical approximation, we conclude that second-order space accuracy is important for ε close to one, while second-order time accuracy is important for ε close to zero.

6.2. *Order of accuracy assessment in one dimension*

We consider a smooth solution from [74] with the following initial data

$$\rho(0,x) = 1 - \frac{\varepsilon}{2}\,\omega\left(\frac{2}{0.25}\left(x - \frac{1}{2}\right)\right) \qquad \text{and} \qquad u(0,x) = 1 + \frac{\varepsilon}{2}\,\omega\left(\frac{2}{0.25}\left(x - \frac{1}{2}\right)\right),$$

on the space domain $[0,1]$ and where the function ω is given by $\omega(z) = \left(\frac{2-|z|}{2}\right)^4 (1 + 2|z|)$ if $|z| \leq 2$, and 0 otherwise. If $\gamma = 3$, see [74], both Riemann invariants are solution to the following Burgers equations:

$$\begin{cases} \partial_t \phi_+ + \phi_+ \partial_x \phi_+ = 0, \\ \partial_t \phi_- + \phi_- \partial_x \phi_- = 0. \end{cases}$$

Solving the above system requires a nonlinear equation solver, such as Newton's method.

For small enough time, the exact solution $(\rho, \rho u)$ is as smooth as the initial data. We use it to determine the Dirichlet boundary conditions for the four schemes and to compute the errors between the approximate solutions and the exact solution. We measure the L^∞ errors for the density and the momentum as follows:

$$e^n_\infty(\rho) = \max_j \left|\rho^n_j - (\rho_{ex})^n_j\right|, \qquad e^n_\infty(\rho u) = \max_j \left|(\rho u)^n_j - ((\rho u)_{ex})^n_j\right|, \tag{30}$$

where ${}^t((\rho_{ex})_j^n, ((\rho u)_{ex})_j^n)$ is the exact solution at time t^n in the cell of center x_j. The time at which the errors are computed are $t_{end} = 0.007$s for $\varepsilon = 1$, $t_{end} = 0.005$s for $\varepsilon = 10^{-2}$ and $t_{end} = 0.0005$s for $\varepsilon = 10^{-4}$. For the four schemes, the density and momentum L^∞ errors are displayed in Figure 9 in logarithmic scale with respect to the number of discretization cells.

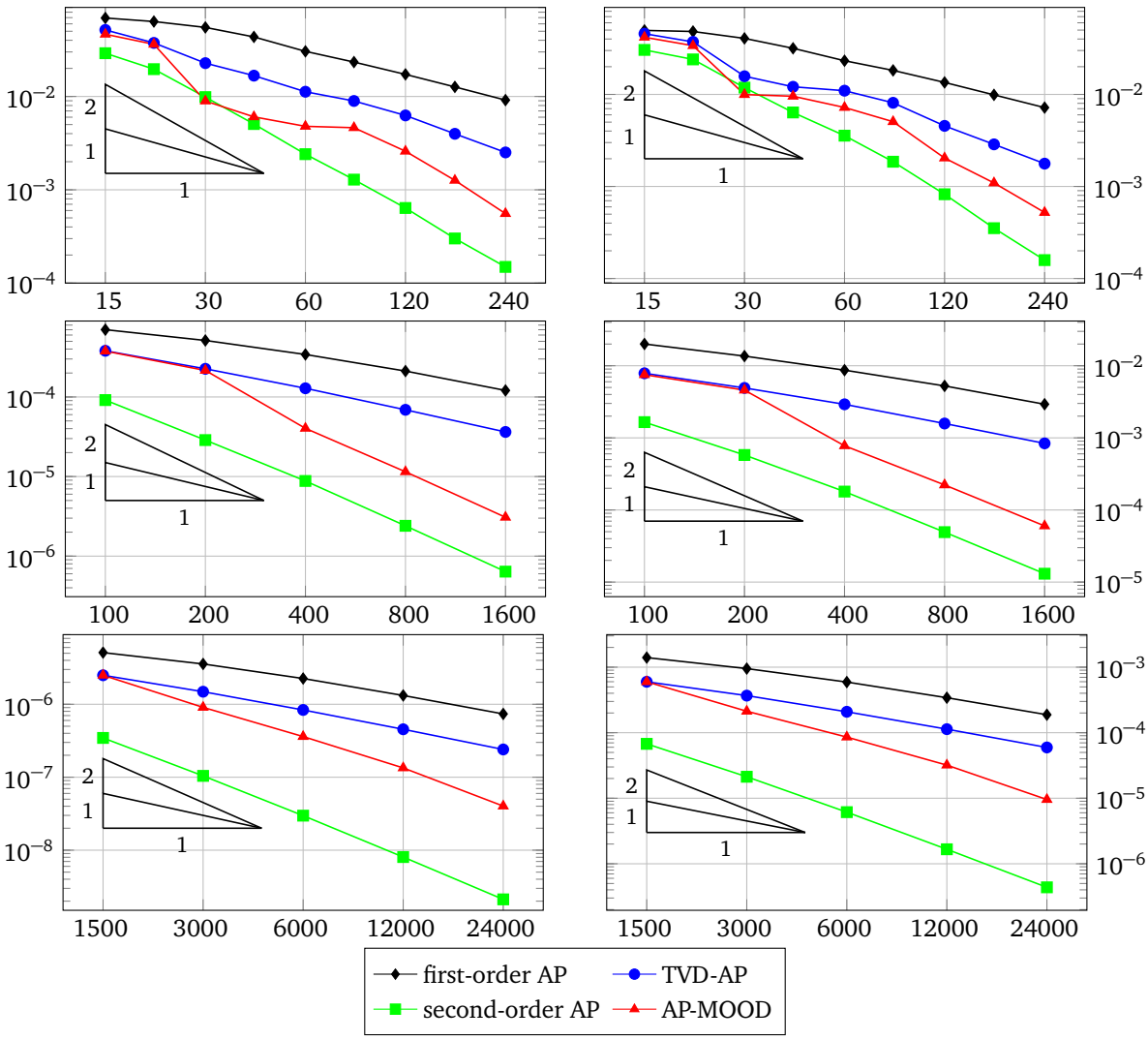

Figure 9: L^∞ error curves for the numerical approximations of the smooth solution (Section 6.2) obtained with the initial data (30). The horizontal axis records the number of cells, while the vertical axis corresponds to the errors produced by the four schemes under consideration. The slopes correspond to the orders of accuracy of the schemes. From top to bottom, we take $\varepsilon = 1$ with $t_{end} = 7 \times 10^{-3}$s, $\varepsilon = 10^{-2}$ with $t_{end} = 5 \times 10^{-3}$s and $\varepsilon = 10^{-4}$ with $t_{end} = 5 \times 10^{-4}$s. The left panels record the density errors and the right panels display the momentum errors.

For all values of ε, the first-order AP scheme and the second-order AP scheme are respectively of order 1 and 2, as expected. In addition, we note that the TVD-AP scheme is also numerically first-order accurate or barely larger but with an L^∞ error which is always lower than the one of the first-order method. For $\varepsilon \in \{10^{-2}, 10^{-4}\}$, the AP-MOOD scheme is numerically of order two in spite of the slope limiter. For $\varepsilon = 1$, the AP-MOOD scheme is of order more than one but less than two, with an L^∞ error always smaller than the one of the first-order method.

Next, we plot in Figure 10 the errors produced by the four schemes as a function of ε. Three fixed grid resolutions are considered: $L = 300$, 7500 and 20000 cells for the left, middle and right panels respectively. Here, we observe that the errors of the four schemes decrease monotonically when ε decreases, unless machine precision is reached.

Generally, the AP-MOOD scheme errors are smaller than the ones from the TVD-AP scheme unless the mesh is too coarse for small ε. As expected, the AP-MOOD errors are larger than the ones from the second-order scheme. Note that the non-monotonic behavior of the AP-MOOD results is probably due to the fact that, for large ε, the error is due to the explicit treatment, while for small ε the implicit treatment of the scheme is to be blamed for this loss of accuracy. Those two errors are of different natures and magnitudes, and, as observed, they may not necessarily reconnect monotonically.

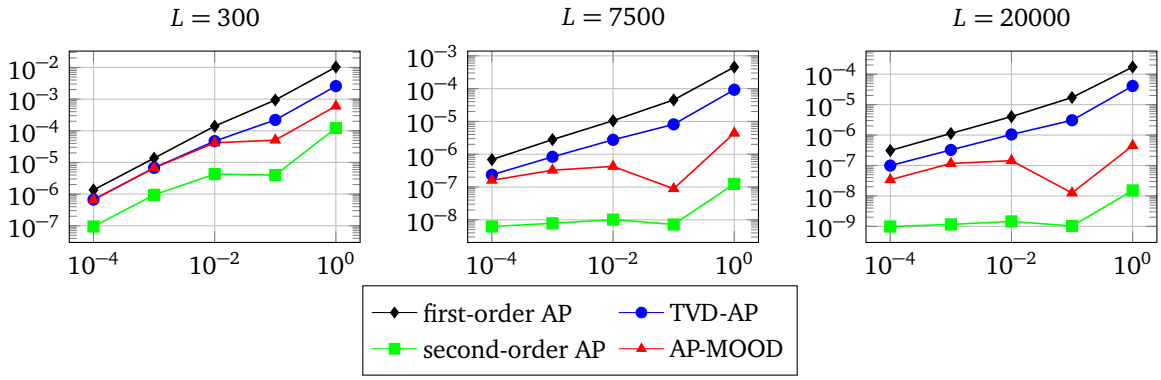

Figure 10: L^∞ error curves for the numerical approximation of the smooth solution (Section 6.2) obtained for the initial data (30). The horizontal axis records the values of ε, while the vertical axis corresponds to the errors produced by the four schemes under consideration. From left to right, we take 300, 7500 and 20000 discretization cells. The time discretization is tied to the number of cells by the CFL condition.

6.3. *Validation and asymptotic stability in one dimension*

We now consider the problem introduced by Degond and Tang in [18]. It consists in several interacting Riemann problems. The initial data are given on the space domain $[0, 1]$ by

$$\rho(0,x) = \begin{cases} 2 & \text{if } x \in [0, 0.2], \\ 2+\varepsilon & \text{if } x \in (0.2, 0.3], \\ 2 & \text{if } x \in (0.3, 0.7], \\ 2-\varepsilon & \text{if } x \in (0.7, 0.8), \\ 2 & \text{if } x \in [0.8, 1], \end{cases} \quad \text{and} \quad (\rho u)(0,x) = \begin{cases} 1-\varepsilon/2 & \text{if } x \in [0, 0.2], \\ 1 & \text{if } x \in (0.2, 0.3], \\ 1+\varepsilon/2 & \text{if } x \in (0.3, 0.7], \\ 1 & \text{if } x \in (0.7, 0.8), \\ 1-\varepsilon/2 & \text{if } x \in [0.8, 1], \end{cases} \tag{31}$$

supplemented by periodic boundary conditions. We choose $\gamma = 1.4$. Here, the goal is to validate the proposed schemes in both the compressible and the incompressible regimes. The reference solution is computed with the first-order AP scheme on a refined mesh in space and time. Figure 11 reports the results for the density on the left and the momentum on the right for $\varepsilon = 1$ and $L = 100$ discretization cells with final time $t_{end} = 0.075$. In the top panels of Figure 12, we display the solution for $\varepsilon = 10^{-4}$ and $t_{end} = 0.0015$ obtained with 1500 cells. In the bottom panels, we have refined the space-time mesh to study the convergence of the numerical approximations.

As in the previous case, the first-order AP scheme is very diffusive and it smears out all shock waves. The second-order AP scheme yields a less diffusive approximation, but it is not TVD because of overshoots and oscillations, while the TVD-AP and AP-MOOD schemes decrease the diffusion, and therefore greatly improve the numerical approximation compared to the first-order AP scheme.

In Figure 12, we observe that the first-order AP scheme projects the approximate solution onto the incompressible limit and avoids computing the small structures and the fast waves present in the reference solution. However, the second-order and the AP-MOOD schemes appropriately capture the micro-structure of the solution, still allowing for much larger time steps. Therefore, if one is interested in the small structures close to the incompressible limit, then high-order numerical schemes seem to be highly relevant.

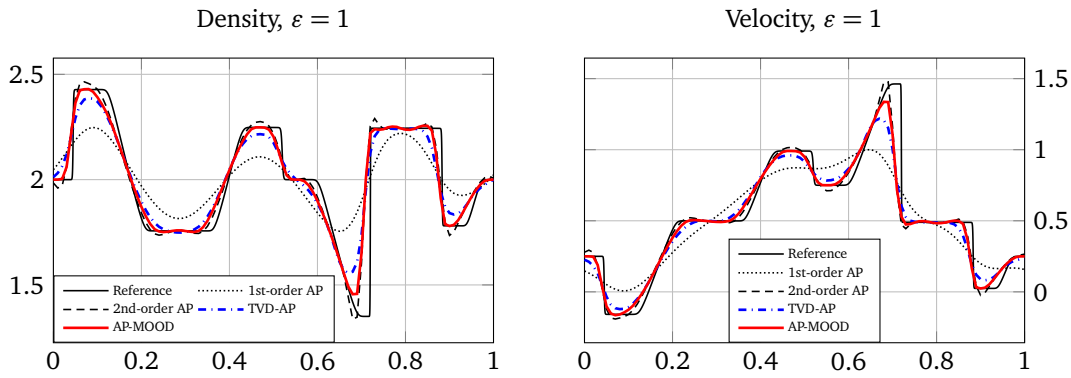

Figure 11: Degond-Tang experiment (Section 6.3) with the initial conditions (31). We take $\varepsilon = 1$ and 100 discretization cells; the results are displayed as functions of space at time $t_{end} = 7.5 \times 10^{-2}$s. The left panel shows the density ρ while the right panel displays the velocity u.

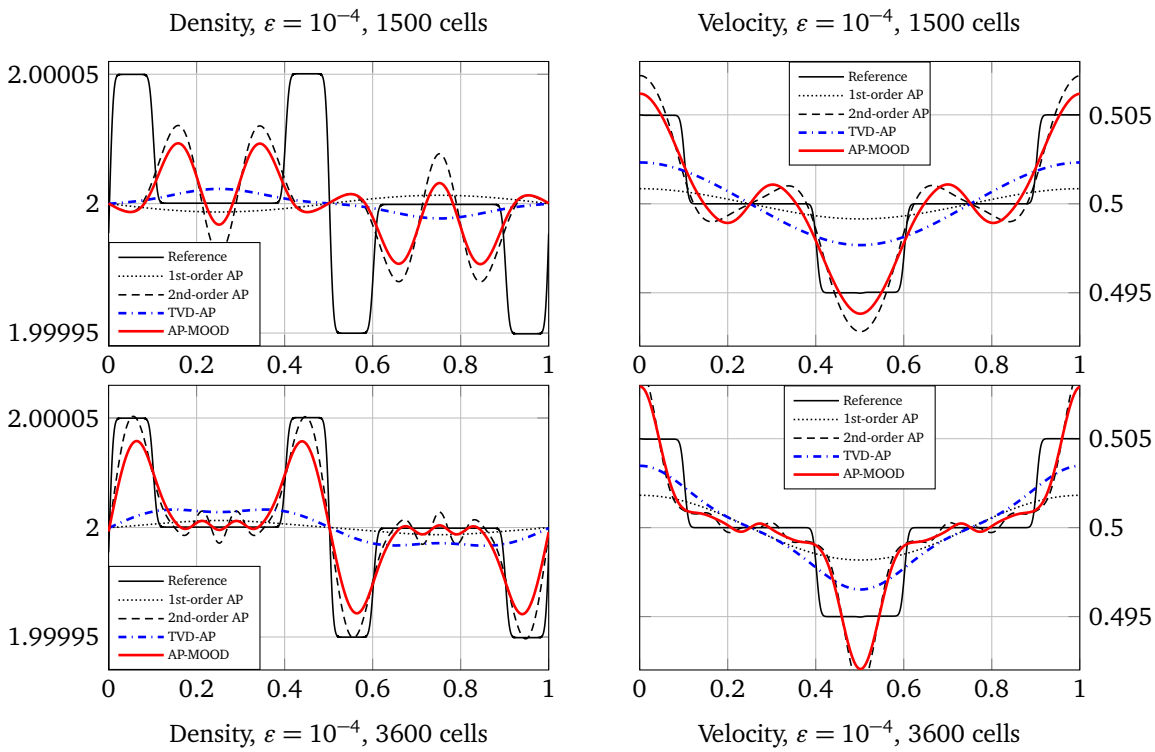

Figure 12: Degond-Tang experiment (Section 6.3) with the initial conditions (31). In the four panels, we set $\varepsilon = 10^{-4}$ and we display the numerical results of the four schemes as functions of space at time $t_{end} = 1.5 \times 10^{-3}$s. We take 1500 discretization cells in the top panels and 3600 cells in the bottom panels. The left panels show the density ρ while the right panels display the velocity u.

6.4. *Order of accuracy in two dimensions*

Now, we measure the order of accuracy of the scheme in two space dimensions. We consider $\gamma = 1$ and the following smooth exact solution of the isentropic Euler system (1):

$$\begin{aligned}
\rho_{ex}(x,y,t) &= \rho_\infty - \frac{a^2\varepsilon}{8d} e^{2d(b-\bar{r}(x,y,t)^2)}, \\
u_{ex}(x,y,t) &= u_\infty + a\bar{y}(t)\sqrt{\frac{\gamma}{2}} e^{d(b-\bar{r}(x,y,t)^2)} \left(\rho_{ex}(x,y,t)\right)^{\frac{\gamma}{2}-1}, \\
v_{ex}(x,y,t) &= v_\infty - a\bar{x}(t)\sqrt{\frac{\gamma}{2}} e^{d(b-\bar{r}(x,y,t)^2)} \left(\rho_{ex}(x,y,t)\right)^{\frac{\gamma}{2}-1},
\end{aligned} \tag{32}$$

where we have set $\bar{r}(x,y,t)^2 = \bar{x}(t)^2 + \bar{y}(t)^2$, with $\bar{x}(t) = x - x_0 - u_\infty t$, $\bar{y}(t) = y - y_0 - v_\infty t$. This exact solution corresponds to a vortex initially centered at ${}^t(x_0, y_0)$ and moving with the phase velocity ${}^t(u_\infty, v_\infty)$. For the numerical simulation, we take $\rho_\infty = 1$, $a = 1$, $b = 0$, $d = 2$, $x_0 = 0$, $y_0 = 0$ and ${}^t(u_\infty, v_\infty) = {}^t(1, 0)$. The space domain is $[-1.5, 2.5] \times [-2, 2]$. The simulations are carried out for three different values of the squared Mach number ε ($\varepsilon = 1$, $\varepsilon = 10^{-2}$, $\varepsilon = 10^{-4}$) until the final physical time $t_{end} = 1$s. To assess the numerical order of accuracy, we compute the following L^∞ errors for several uniform meshes :

$$e^n_\infty(\rho) = \max_{j,k} \left| \rho^n_{j,k} - (\rho_{ex})^n_{j,k} \right| \quad \text{and} \quad e^n_\infty(\rho U) = \max_{j,k} \left| \left(\rho \sqrt{u^2 + v^2}\right)^n_{j,k} - \left(\rho_{ex} \sqrt{u^2_{ex} + v^2_{ex}}\right)^n_{j,k} \right|.$$

For the four schemes, the errors are collected in Table 2 for $\varepsilon = 1$, Table 3 for $\varepsilon = 10^{-2}$ and Table 4 for $\varepsilon = 10^{-4}$. In addition, we display error lines in Figure 13.

	1st-order AP		TVD-AP		2nd-order AP		AP-MOOD	
N	$e^n_\infty(\rho)$	order	$e^n_\infty(\rho)$	order	$e^n_\infty(\rho)$	order	$e^n_\infty(\rho)$	order
625	4.30e-02	—	1.93e-02	—	8.84e-03	—	1.04e-02	—
2500	3.36e-02	0.35	6.05e-03	1.67	1.66e-03	2.41	2.14e-03	2.28
10000	2.20e-02	0.61	2.08e-03	1.54	2.87e-04	2.53	6.31e-04	1.76
40000	1.30e-02	0.76	7.63e-04	1.45	5.63e-05	2.35	1.80e-04	1.81
N	$e^n_\infty(\rho U)$	order	$e^n_\infty(\rho U)$	order	$e^n_\infty(\rho U)$	order	$e^n_\infty(\rho U)$	order
625	1.07e-01	—	4.61e-02	—	1.62e-02	—	2.26e-02	—
2500	7.59e-02	0.50	1.25e-02	1.88	3.02e-03	2.42	4.40e-03	2.36
10000	4.73e-02	0.68	5.19e-03	1.27	5.33e-04	2.50	1.47e-03	1.59
40000	2.69e-02	0.81	2.54e-03	1.03	1.09e-04	2.29	4.84e-04	1.60

Table 2: Smooth unsteady vortex experiment (Section 6.4): comparisons of the density and momentum L^∞ errors between the exact solution (32) and the four numerical approximations, for several space discretizations, with $\varepsilon = 1$, and at time $t_{end} = 1$s.

	1st-order AP		TVD-AP		2nd-order AP		AP-MOOD	
N	$e^n_\infty(\rho)$	order	$e^n_\infty(\rho)$	order	$e^n_\infty(\rho)$	order	$e^n_\infty(\rho)$	order
625	5.58e-04	—	3.57e-04	—	1.57e-04	—	2.46e-04	—
2500	5.16e-04	0.11	1.41e-04	1.34	3.31e-05	2.25	4.49e-05	2.46
10000	4.20e-04	0.30	4.94e-05	1.52	4.68e-06	2.82	1.68e-05	1.42
40000	3.02e-04	0.48	1.55e-05	1.67	6.33e-07	2.89	4.37e-06	1.94
N	$e^n_\infty(\rho U)$	order	$e^n_\infty(\rho U)$	order	$e^n_\infty(\rho U)$	order	$e^n_\infty(\rho U)$	order
625	1.51e-01	—	7.79e-02	—	3.19e-02	—	3.88e-02	—
2500	1.28e-01	0.24	2.84e-02	1.46	6.04e-03	2.40	6.81e-03	2.51
10000	9.52e-02	0.43	9.35e-03	1.60	8.50e-04	2.83	1.38e-03	2.30
40000	6.31e-02	0.59	2.81e-03	1.74	1.15e-04	2.89	4.57e-04	1.59

Table 3: Smooth unsteady vortex experiment (Section 6.4): comparisons of the density and momentum L^∞ errors between the exact solution (32) and the four numerical approximations, for several space discretizations, with $\varepsilon = 10^{-2}$, and at time $t_{end} = 1$s.

From these results, we draw similar conclusions as in the 1D case. The slopes and errors of the TVD-AP and AP-MOOD schemes lie in between the first- and the second-order slopes and errors.

6.5. Asymptotic consistency of the schemes in two dimensions

Finally, we perform a 2D validation experiment, initially described in [75] and used more recently in [8]. It is particularly relevant since, for small values of ε, we can compare the compressible numerical approximations to an

	1st-order AP		TVD-AP		2nd-order AP		AP-MOOD	
N	$e^n_\infty(\rho)$	order	$e^n_\infty(\rho)$	order	$e^n_\infty(\rho)$	order	$e^n_\infty(\rho)$	order
625	2.42e-05	—	1.12e-05	—	5.32e-06	—	6.33e-06	—
2500	2.21e-05	0.13	1.27e-05	-0.18	1.75e-06	1.60	1.79e-06	1.82
10000	1.17e-05	0.91	2.97e-06	2.10	8.31e-07	1.08	7.88e-07	1.19
40000	9.33e-06	0.33	2.06e-06	0.53	1.19e-07	2.80	1.18e-07	2.74
N	$e^n_\infty(\rho U)$	order	$e^n_\infty(\rho U)$	order	$e^n_\infty(\rho U)$	order	$e^n_\infty(\rho U)$	order
625	1.61e-01	—	8.81e-02	—	3.74e-02	—	4.43e-02	—
2500	1.43e-01	0.16	4.40e-02	1.00	8.76e-03	2.09	9.17e-03	2.27
10000	1.17e-01	0.29	1.72e-02	1.36	1.65e-03	2.41	1.75e-03	2.39
40000	8.59e-02	0.45	5.69e-03	1.59	3.06e-04	2.43	3.05e-04	2.52

Table 4: Smooth unsteady vortex 2D experiment (Section 6.4): comparisons of the density and momentum L^∞ errors between the exact solution (32) and the four numerical approximations, for several space discretizations, with $\varepsilon = 10^{-4}$, and at time $t_{end} = 1$s.

approximate solution of the incompressible Euler equations. That way, we can measure the asymptotic consistency of our approximations in the low Mach number limit.

The initial data are well-prepared. Indeed, on the space domain $[0, 2\pi]^2$, we take a constant density $\rho = \pi/15$, and the initial incompressible velocity field $U = (u, v)$ is given by:

$$u(x, y, 0) = \begin{cases} \tanh((y - \pi/2)/\rho), & \text{if } y \leq \pi, \\ \tanh((3\pi/2 - y)/\rho), & \text{otherwise,} \end{cases} \qquad v(x, y, 0) = 0.05 \sin(x).$$

In addition, we take $\gamma = 1$ and we prescribe periodic boundary conditions for the compressible Euler system.

To determine the incompressible approximate solution, we consider the vorticity formulation of the incompressible Euler system, given by:

$$\partial_t \omega + U \cdot \nabla \omega = 0, \tag{33}$$

and we recall that the vorticity ω is given by $\omega = \partial_x v - \partial_y u$. Since $\nabla \cdot U = 0$, there exists a stream function ψ such that $U = {}^t(\partial_y \psi, -\partial_x \psi)$ and $-\Delta\psi = \omega$. From these observations, we can obtain a reference solution. We compute the time evolution of the vorticity by repeating the following three steps: we first compute the stream function ψ, then the associated velocity field, and finally the time update of the vorticity with (33). To solve the Poisson equation $-\Delta\psi = \omega$, we use a classical discretization of the Laplace operator, and we prescribe periodic boundary conditions. Since this leads to a singular system, we also impose that the stream function has a null average. This does not alter the rest of the procedure since we are only interested in the derivatives of ψ. The velocity is then obtained by an application of a centered gradient discretization, and an upwind finite difference scheme provides an approximate solution for (33). Periodic boundary conditions are prescribed in both of these steps.

We stress that the reference solution is obtained from the incompressible Euler equations while the schemes under consideration approximately solve the compressible Euler system with a very small Mach number. The results are displayed in Figure 14. We take $\varepsilon = 10^{-5}$ and $t_{end} = 6$s to compare the numerical solutions provided by the four schemes for the compressible Euler system with the reference incompressible solution. The mesh is constituted of 200×200 cells.

We can see that the first-order scheme loses the main structure of the solution (it is worth noting that, on a much finer space-time grid, the structure is captured by the first-order scheme). The limited TVD-AP scheme provides a smeared numerical approximation, while the AP-MOOD and second-order schemes yield similar numerical solutions. We note that, for these schemes, the main structure of the solution is captured. However, the small central structures are smeared because the grid is too coarse. Overall, the proposed compressible schemes offer a convincing approximation of the incompressible solution when ε is small enough.

Now, we carry out this experiment for $\varepsilon = 1$. First, we compute a reference solution with the first-order AP scheme on a fine 400×400 grid at the final time $t_{end} = 10$s. In Figure 15, we compare the vorticity computed by the four schemes on a coarse 40×40 grid to this reference solution.

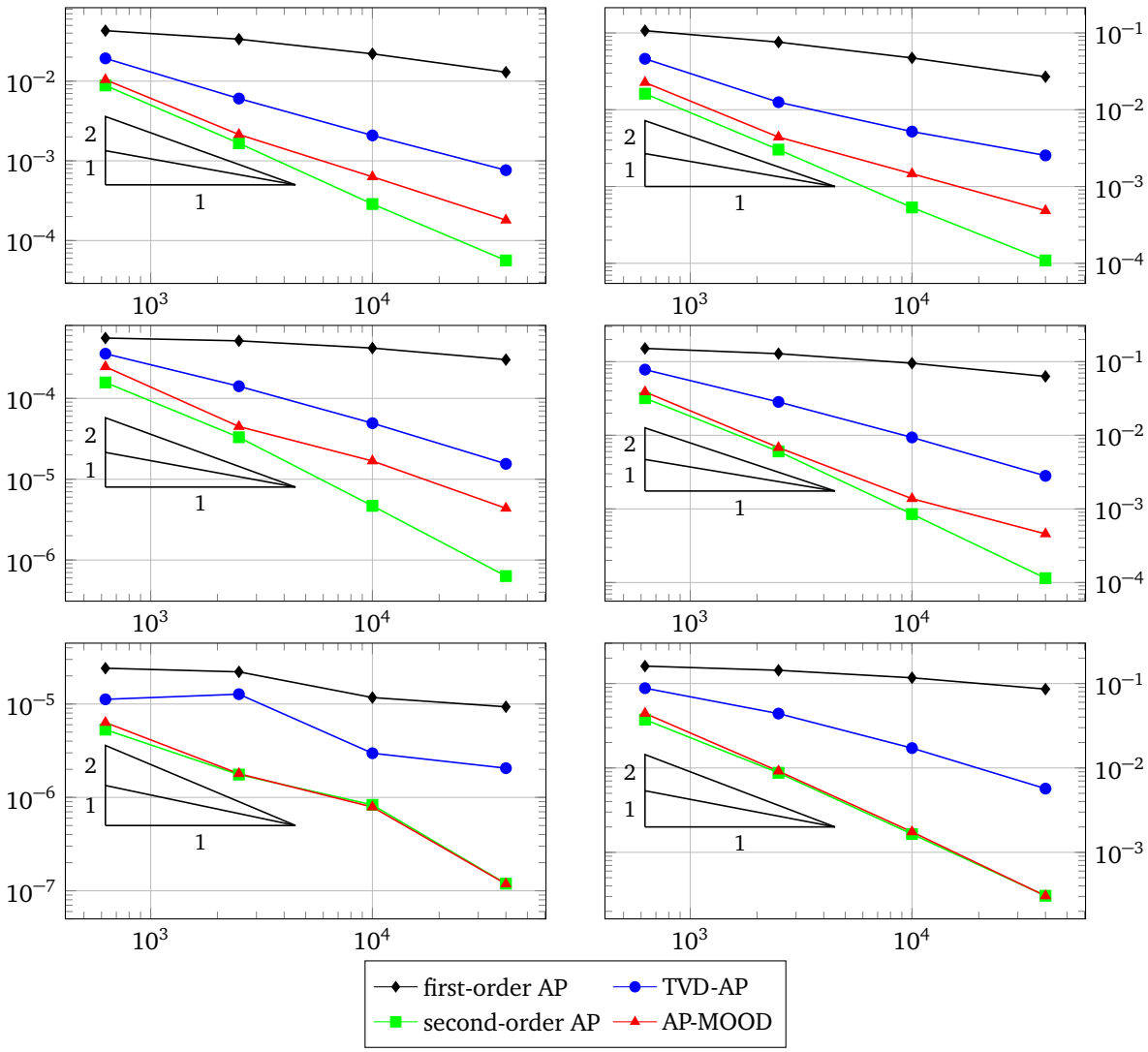

Figure 13: L^∞ error curves for the 2D smooth unsteady vortex (Section 6.4), drawn at time $t_{end} = 1$s. The horizontal axis records the number of cells, while the vertical axis corresponds to the errors produced by the four schemes under consideration, tested against the exact solution (32). The slopes correspond to the orders of accuracy of the schemes. From top to bottom, we take $\varepsilon = 1$, $\varepsilon = 10^{-2}$ and $\varepsilon = 10^{-4}$. The left panels record the density errors and the right panels display the momentum errors.

We note that the main structures of the reference solution are captured by the second-order and the AP-MOOD scheme, with the TVD-AP scheme being slightly more diffusive. However, the first-order scheme is so diffusive that it destroys most of the structures. In the bottom left corner of Figure 15, we have added a zoom on the domain $[2.35, 3.85] \times [4.4, 5]$ of the reference and the second-order solutions. We note that the very fine structure present in this domain is smeared by the second-order scheme due to the use of too coarse a mesh.

7. Conclusion

In this work, we have developed a new numerical method for describing physical problems in which incompressible and compressible regimes coexist. Since non-physical oscillations cannot be avoided for non-restrictive CFL conditions larger than the ones imposed by explicit methods, we have constructed a new method based on the coupling of first-order with second-order in time and space schemes. This approach has allowed us to develop a highly

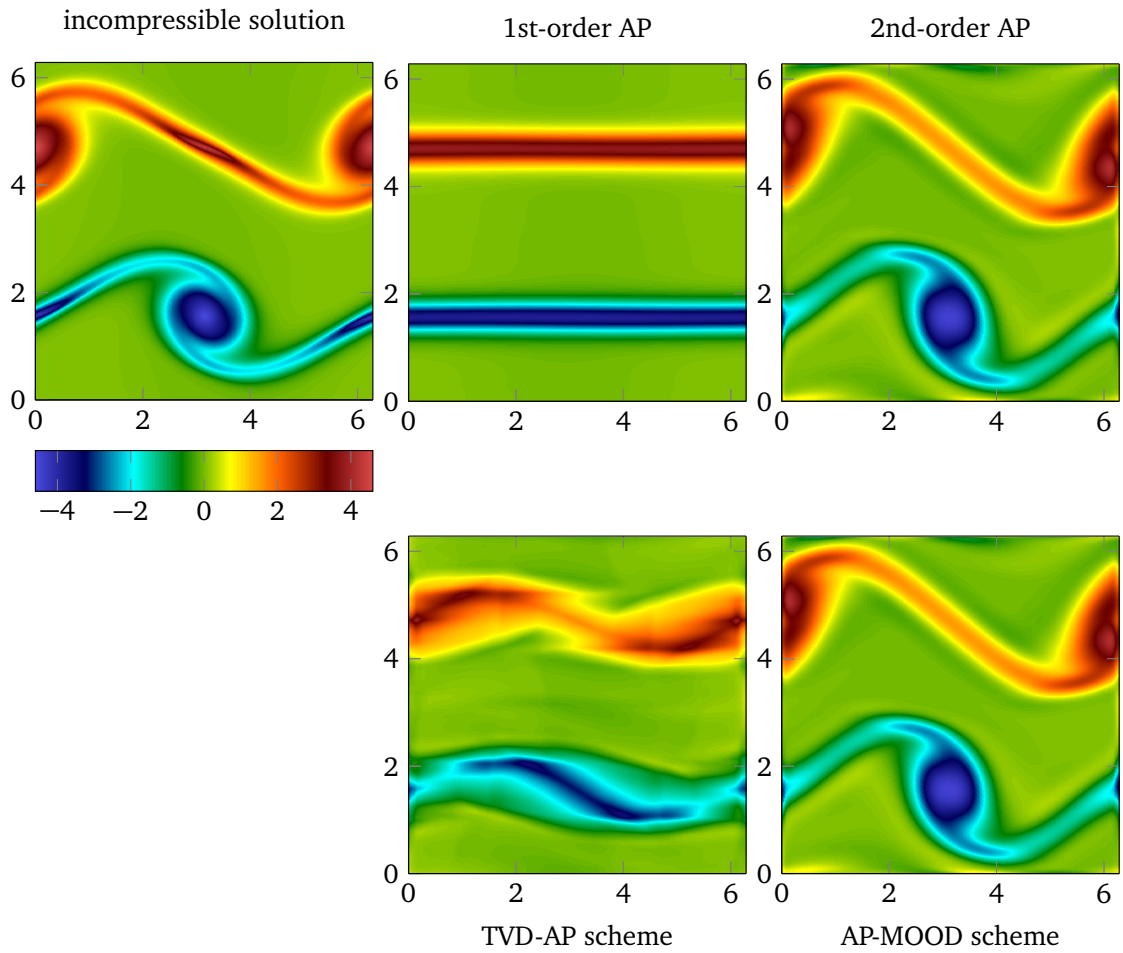

Figure 14: Numerical approximations of the vorticity $\partial_x v - \partial_y u$ for the double shear layer experiment (Section 6.5) at time $t_{end} = 6$s. All five simulations are carried out on a Cartesian mesh with $200 \times 200 = 40000$ cells. The reference solution is obtained by solving the incompressible Euler system (33). To get a relevant approximation of the incompressible solution, the four compressible schemes under consideration are used in an almost incompressible regime, i.e. with a very small value of the Mach number. We take $\varepsilon = 10^{-5}$, which corresponds to a Mach number equal to $\sqrt{\varepsilon} \approx 3.2 \times 10^{-3}$.

accurate and asymptotic-preserving scheme, which additionally enjoys the TVD and the L^∞-stability properties independently of the Mach number. Then, the introduction of limiters enabled a passage from the second-order to the TVD method only when strictly necessary, further improving the overall accuracy. For the scheme presented, the stability constraints do not depend on the value of the Mach number. In addition, it degenerates into a consistent highly accurate discretization of the incompressible system in the low Mach number limit. Numerical experiments supported the proposed analysis. In particular, we showed that the method developed is able to deal with situations in which the fast sound waves of the low Mach regions play only a weak role in the description of the problem. In these cases, in which the accurate resolution of the fast waves is not requested, the numerical scheme permits the use of large time steps, independently of the small Mach number values, and to avoid their detailed resolution. Since, it is well known that implicit discretizations together with large time steps introduce large numerical dissipation, high-order extensions of the present scheme are very important especially for the high Mach regions. For this reason, in the future, we aim at focusing on the generalization of such techniques to the case of TVD schemes which couple AP schemes of order higher than two with first-order in time AP methods. Moreover, we aim at exploring more in depth the use of limiters since, in some cases, some small oscillations remain present for the limited method. Local coupling techniques between the schemes of different orders could also largely improve the results obtained; they are now the

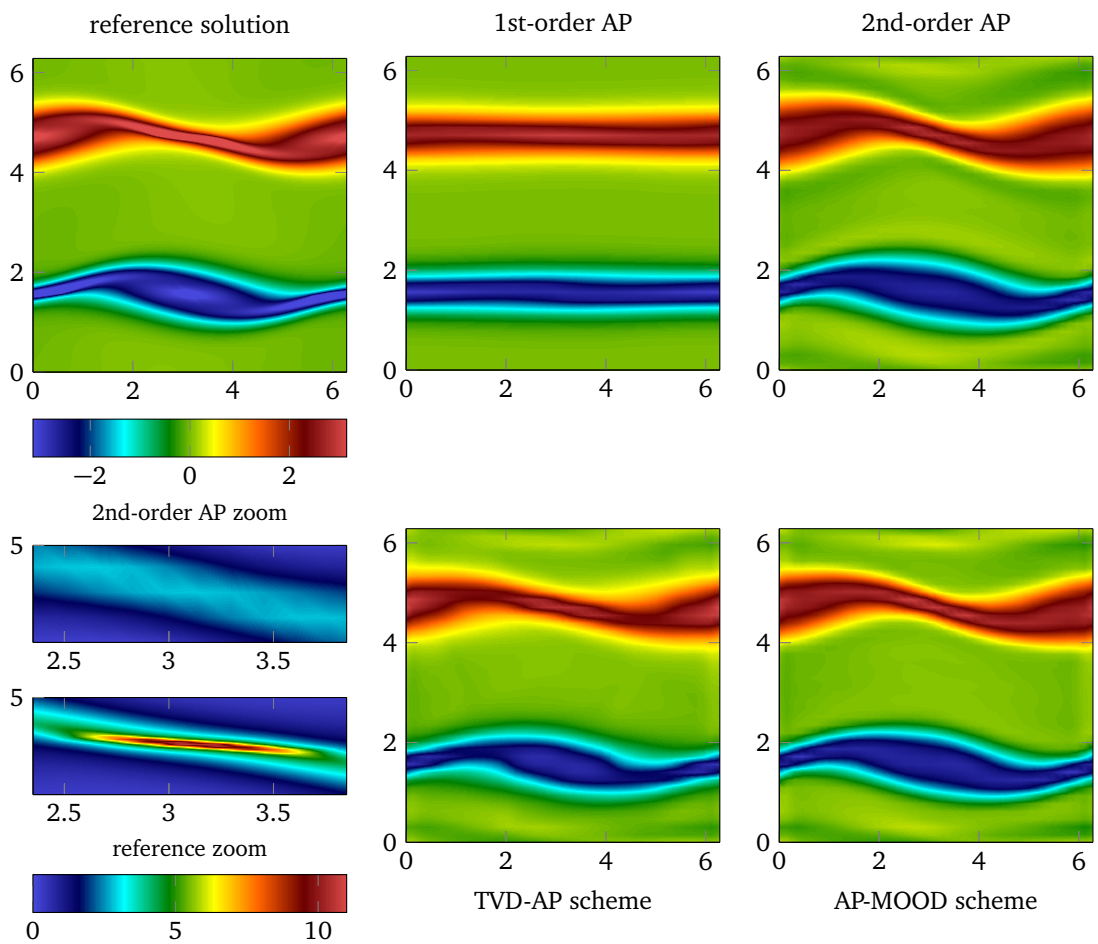

Figure 15: Numerical approximations of the vorticity $\partial_x v - \partial_y u$ for the double shear layer experiment (Section 6.5), with $\varepsilon = 1$ and at time $t_{end} = 6$s. The reference solution is obtained by using the first-order AP scheme with 400×400 cells, while the other approximate solutions are made with $40 \times 40 = 1600$ cells. The bottom left of this figure contains a zoom on a very small structure smeared by the coarse mesh but present in the reference solution. The color legend in the bottom left corner is only applied to this zoom.

subject of investigations. An extension to the full Euler equations is under study based on the first-order AP scheme presented in [22].

Acknowledgments

G. Dimarco, V. Michel-Dansac and M.H. Vignal were supported by the French ANR project MOONRISE ANR-14-CE23-0007. The material of this work has been gathered during SHARK-FV conference (*Sharing Higher-order Advanced Know-how on Finite Volume* `http://www.SHARK-FV.eu/` held in 2017.

References

[1] T. Alazard, Incompressible limit of the nonisentropic Euler equations with the solid wall boundary conditions. Adv. Differential Equations, 10(1), 19–44, 2005.
[2] K. Asano, On the incompressible limit of the compressible Euler equation. Japan J. Appl. Math. 4, 455–488, 1987.
[3] U. M. Ascher, S. J. Ruuth, R. J. Spiteri, Implicit-explicit Runge-Kutta methods for time-dependent partial differential equations. Appl. Numer. Math. 25(2-3) 151–167, 1997, Special issue on time integration (Amsterdam, 1996).
[4] G. Bispen, M. Lukáčová-Medvid'ová, L. Yelash, Asymptotic preserving IMEX finite volume schemes for low Mach number Euler equations with gravitation, J. Comput. Phys. 335, 222–248, 2017.

[5] M. Boger, F. Jaegle, R. Klein, C.-D. Munz, Coupling of compressible and incompressible flow regions using the multiple pressure variables approach. Math. Methods Appl. Sci. 38 (2015), no. 3, 458-477.
[6] S. Boscarino, G. Russo, On a class of uniformly accurate IMEX Runge-Kutta schemes and applications to hyperbolic systems with relaxation, SIAM J. Sci. Comput. 31(3), 1926–1945, 2009.
[7] S. Boscarino, G. Russo, Flux-explicit IMEX Runge-Kutta schemes for hyperbolic to parabolic relaxation problems, SIAM J. Numer. Anal. 51(1), 163–190, 2013.
[8] S. Boscarino, G. Russo, L. Scandurra, All Mach Number Second Order Semi-Implicit Scheme for the Euler Equations of Gasdynamics, preprint.
[9] C. Bresten, S. Gottlieb, Z. Grant, D. Higgs, D. I. Ketcheson, A. Németh, Explicit strong stability preserving multistep Runge–Kutta methods. Math. Comp. 86, 747–769, 2017.
[10] C. Chalons, M. Girardin, S. Kokh, Large time step and asymptotic preserving numerical schemes for the gas dynamics equations with source terms, SIAM J. Sci. Comput. 35,2874–2902, 2013.
[11] C. Chalons, M. Girardin, S. Kokh, An all-regime Lagrange-Projection like scheme for the gas dynamics equations on unstructured meshes, Communications in Computational Physics (CICP), 20(1), 188–233, 2016.
[12] S. Clain, S. Diot, R. Loubère, A high-order finite volume method for systems of conservation laws—Multi-dimensional Optimal Order Detection (MOOD), J. Comput. Phys. 230(10), 4028–4050, 2011.
[13] Ph. Colella, K. Pao, A projection method for low speed flows, J. Comp. Phys. 149, 245–269, 1999.
[14] S. Conde, S. Gottlieb, Z. J. Grant, J. N. Shadid, Implicit and Implicit-Explicit Strong Stability Preserving Runge-Kutta Methods with High Linear Order, J. Sci. Comput., 73, 667–690, 2017.
[15] E. M. Constantinescu, A. Sandu, Optimal explicit strong-stability-preserving general linear methods, SIAM J. Sci. Comput. 32, 3130–3150, 2010.
[16] F. Cordier, P. Degond, A. Kumbaro, An Asymptotic-Preserving all-speed scheme for the Euler and Navier Stokes equations, J. Comp. Phys. 231, 5685–5704, 2012.
[17] P. Degond, F. Deluzet, A. Sangam, M.-H. Vignal, An Asymptotic Preserving Scheme for the Euler equations in a strong magnetic field, Comp. Phys. 228, 3540–3558, 2009.
[18] P. Degond, M. Tang, All speed scheme for the low Mach number limit of the isentropic Euler equations. Commun. Comput. Phys. 10(1), 1–31, 2011.
[19] P. Degond, S. Jin, J.-G. Liu, Mach-number uniform asymptotic-preserving gauge schemes for compressible flows. Bull. Inst. Math. Acad. Sin. (N.S.) 2 (2007), no. 4, 851-892.
[20] S. Dellacherie, Analysis of Godunov type schemes applied to the compressible Euler system at low Mach number, J. Comp. Phys. 229, 978-1016, 2010.
[21] S. Dellacherie, J. Jung, P. Omnes, Preliminary results for the study of the Godunov Scheme Applied to the Linear Wave Equation with Porosity at Low Mach Number, ESAIM ProcS. 52, 105-126, 2015.
[22] G. Dimarco, R. Loubère, M.-H. Vignal, Study of a new asymptotic preserving scheme for the Euler system in the low Mach number limit, SIAM J. Sci. Comput., 39(5), A2099–A2128, 2017.
[23] G. Dimarco, L. Pareschi, Asymptotic-preserving IMEX Runge-Kutta methods for nonlinear kinetic equations, SIAM J. Num. Anal. 1064–1087, 2013.
[24] G. Dimarco, L. Pareschi, High order asymptotic preserving schemes for the Boltzmann equation, Comptes Rendus Mathematique 350, 9, 481–486, 2012.
[25] S. Diot, S. Clain, R. Loubère, Improved detection criteria for the multi-dimensional optimal order detection (MOOD) on unstructured meshes with very high-order polynomials, Comput. & Fluids, 64, 43–63, 2012.
[26] S. Diot, R. Loubère, and S. Clain, The multidimensional optimal order detection method in the three-dimensional case: very high-order finite volume method for hyperbolic systems, Internat. J. Numer. Methods Fluids, 73(4), 362–392, 2013.
[27] R. Eymard, T. Gallouët, R. Herbin, Finite volume methods, Handbook of numerical analysis, Vol. VII, 713–1020, North-Holland, Amsterdam, 2000.
[28] L. Ferracina, M. N. Spijker, Stepwize restrictions for the total-variation-diminishing property in general Runge-Kutta mathods, SIAM J. Numer. Anal. 42, 1073–1093, 2004.
[29] N. Grenier, J.-P. Vila, P. Villedieu, An accurate low-Mach scheme for a compressible two-fluid model applied to free-surface flows, J. Comp. Phys. 252, 1–19, 2013.
[30] S. Gottlieb, C.-W. Shu, E. Tadmor, Strong stability-preserving high-order time discretization methods, SIAM Rev. 43(1), 89–112, 2001.
[31] H. Guillard, A. Murrone, On the behavior of upwind schemes in the low Mach number limit : II. Godunov type schemes, Comp. & Fluids, 33, 655–675, 2004.
[32] H. Guillard, C. Viozat, On the behavior of upwind schemes in the low Mach limit, Comp. & Fluid, 28, 63–86, 1999.
[33] J. Haack, S. Jin, J.G. Liu, An all-speed asymptotic-preserving method for the isentropic Euler and Navier-Stokes equations, Commun. Comput. Phys., 12, 955–980, 2012.
[34] F. H. Harlow, A. Amsden, A numerical fluid dynamics calculation method for all flow speeds, J. Comput. Phys, 8, 197–213, 1971.
[35] D. R. van der Heul, C. Vuik, P. Wesseling, A conservative pressure-correction method for flow at all speeds, Comp. & Fluids, 32 (2003), pp. 1113-1132.
[36] I. Higueras, N. Happenhofer, O. Koch, F. Kupka, Optimized strong stability preserving IMEX Runge-Kutta methods. J. Comput. Appl. Math. 272 (2014), 116-140.
[37] I. Higueras, Representations of Runge-Kutta methods and strong stability preserving methods, SIAM J. Numer. Anal., 43, 924–948, 2005.
[38] R.I. Issa, A.D.Gosman, A.P. Watkins, The computation of compressible and incompressible flow of fluid with a free surface, Phys. Fluids, 8, 2182–2189, 1965.
[39] A. Jameson, S. Yoon, Multigrid solution of the Euler equations using implicit schemes, AIAA Journal, 24 (1986), 1737–1743.
[40] A. Jameson, Solution of the Euler equations for two dimensional transonic flow by a multigrid method, Appl. Math. Comp, 13 (1983),

327–355.
[41] A. Jameson, D.A. Caughey, How Many Steps are Required to Solve the Euler Equations of Steady Compressible Flow: In Search of a Fast Solution Algorithm, AIAA 2001-2673, 15th AIAA Computational Fluid Dynamics Conference, June 11-14, 2001, Anaheim, CA.
[42] D. I. Ketcheson, C. B. Macdonald, S. Gottlieb, Optimal implicit strong stability preserving Runge-Kutta methods. Appl. Numer. Math. 59 (2009), no. 2, 373-392.
[43] W. Kheriji, R. Herbin, J.-C. Latché, Pressure correction staggered schemes for barotropic one-phase and two-phase flows, Comp. & Fluids, 88, 524–542, 2013.
[44] S. Klainerman, A. Majda, Singular limits of quasilinear hyperbolic systems with large parameters and the incompressible limit of compressible fluids, Comm. Pure Appl. Math. 34(4), 481–524, 1981.
[45] S. Klainerman, A. Majda, Compressible and incompressible fluids, Comm. Pure Appl. Math. 35(5), 629–651, 1982.
[46] R. Klein, Semi-implicit extension of a Godunov-type scheme based on low Mach number asymptotics I: One-dimensional flow, J. Comp. Phys., 121, 213–237, 1995.
[47] R. J. LeVeque, Finite volume methods for hyperbolic problems, Cambridge Texts in Applied Mathematics. Cambridge University Press, Cambridge, 2002.
[48] P.-L. Lions, N. Masmoudi, Incompressible limit for a viscous compressible fluid, J. Math. Pures Appl. (9), 77(6), 585–627, 1998.
[49] M.-S. Liou, A sequel to AUSM, Part II: AUSM+-up for all speeds, J. Comput. Phys., 214, 137–170, 2006.
[50] G. Métivier, S. Schochet, The incompressible limit of the non-isentropic Euler equations, Arch. Ration. Mech. Anal., 158(1), 61–90, 2001.
[51] V. Michel-Dansac, G. Dimarco, R. Loubère, and M.-H. Vignal, Total Variation Diminishing implicit-explicit schemes, Work in progress, 2017.
[52] C. D. Munz, S. Roller, R. Klein, K. J. Geratz, The extension of incompressible flow solvers to the weakly compressible regime, Comp. Fluid, 32, 173–196, 2002.
[53] C. D. Munz, M. Dumbser, S. Roller, Linearized acoustic perturbation equations for low Mach number flow with variable density and temperature, J. Comput. Phys., 224, 352–364, 2007.
[54] S. Noelle, G. Bispen, K.R. Arun, M. Lukáčová-Medvid'ová, C. D. Munz, A weakly asymptotic preserving low Mach number scheme for the Euler equations of gas dynamics. SIAM J. Sci. Comput. 36 (2014), no. 6, B989-B1024.
[55] J. H. Park, C. D. Munz, Multiple pressure variables methods for fluid flow at all Mach numbers, Int. J. Numer. Meth. Fluid, 49, 905–931, 2005.
[56] H. Paillère, C. Viozat, A. Kumbaro, I. Toumi, Comparison of low mach number models for natural convection problems. Heat & Mass Tran., 36, 567–573, 2000.
[57] H. Paillère, C. Core, J. Garcia, On the extension of the AUSM+ scheme to compressible two-fluid models, Computers & Fluids, 32 891–916, 2003.
[58] L. Pareschi, G. Russo, Implicit-explicit Runge-Kutta schemes for stiff systems of differential equations, In Recent trends in numerical analysis, volume 3 of Adv. Theory Comput. Math. pages 269–288. Nova Sci. Publ., Huntington, NY, 2001.
[59] L. Pareschi, G. Russo, Implicit-Explicit Runge-Kutta schemes and applications to hyperbolic systems with relaxation, J. Sci. Comput. 25(1-2), 129–155, 2005.
[60] S. V. Patankar, Numerical heat transfer and fluid flow, New York: McGraw-Hill, 1980.
[61] O. Peles, E. Turkel Acceleration Methods for Multi-physics Compressible Flow J. Comput. Phys., 358 (2018) 201–234.
[62] C.-C. Rossow, A Flux-Splitting Scheme for Compressible and Incompressible Flows, J. Comput. Phys., 164, 104–122, 2000
[63] C.-C. Rossow, Convergence acceleration for solving the compressible Navier-Stokes equations, AIAA J., 44, 345-352, 2006.
[64] R.C. Swanson, E. Turkel, C.-C. Rossow, Convergence acceleration of Runge-Kutta schemes for solving the Navier-Stokes equations, J. Comput. Phys., 224, 365–388, 2007.
[65] V.V. Rusanov, Calculation of interaction of non-steady shock waves with obstacles. J. Comput. Math. Phys. USSR 1, 267–279, 1961.
[66] S. Schochet, The compressible Euler equations in a bounded domain: existence of solutions and the incompressible limit, Comm. Math. Phys., 104(1), 49–75, 1986.
[67] J. A. Smoller, J. L. Johnson. Global solutions for an extended class of hyperbolic systems of conservation laws, Arch. Rational Mech. Anal. 32, 169–189, 1969.
[68] H. Song, Energy SSP-IMEX Runge-Kutta methods for the Cahn-Hilliard equation. J. Comput. Appl. Math. 292 (2016), 576-590.
[69] E. F. Toro, Riemann solvers and numerical methods for fluid dynamics. A practical introduction, Springer-Verlag, Berlin, third edition, 2009.
[70] B. van Leer, Towards the Ultimate Conservative Difference Scheme, V. A Second Order Sequel to Godunov's Method, J. Com. Phys. 32, 101–136, 1979.
[71] M. Tang, Second order all speed method for the isentropic Euler equations. Kinet. Relat. Models 5 (2012), no. 1, 155-184.
[72] E. Turkel, Preconditioned methods for solving the incompressible and low speed compressible equations, J. Comp. Phys., 72, 277–298, 1987.
[73] E. Turkel and V.N. Vatsa, Local Preconditioners for Steady State and Dual Time-Stepping, ESAIM: M2AN, 39, 515–536, 2005.
[74] F. Vilar, P.-H. Maire, R. Abgrall, Cell-centered discontinuous Galerkin discretizations for two-dimensional scalar conservation laws on unstructured grids and for one-dimensional Lagrangian hydrodynamics, Comput. & Fluids, 46, 498–504, 2011.
[75] W. E, C.-W. Shu, A Numerical Resolution Study of High Order Essentially Non-oscillatory Schemes Applied to Incompressible Flow, J. Comput. Phys. 110, 39–46, 1994.